

Chapter 2

Nonlinear Spectroscopy

One of the essential advantages that single-mode lasers can offer for high-resolution spectroscopy is the possibility of overcoming the limitation set by Doppler broadening. Several techniques have been developed that are based on selective saturation of atomic or molecular transitions by sufficiently intense lasers.

The population density of molecules in the absorbing level is decreased by optical pumping. This results in a nonlinear dependence of the absorbed radiation power on the incident power. Such techniques are therefore summarized as *nonlinear spectroscopy*, which also includes methods that are based on the simultaneous absorption of two or more photons during an atomic or molecular transition. In the following sections the basic physics and the experimental realization of some important methods of nonlinear spectroscopy are discussed. At first we shall, however, treat the saturation of population densities by intense incident radiation.

2.1 Linear and Nonlinear Absorption

Assume that a monochromatic plane lightwave

$$E = E_0 \cos(\omega t - kz),$$

with the mean intensity

$$I = \frac{1}{2} c \epsilon_0 E_0^2 \text{ [W/m}^2\text{]},$$

passes through a sample of molecules, which absorb on the transition $E_i \rightarrow E_k$ ($E_k - E_i = \hbar\omega$). The power dP absorbed in the volume $dV = A dz$ is then

$$dP = -P_0 \alpha dz = -A I_0 \sigma_{ik} \Delta N dz \text{ [W]}, \quad (2.1a)$$

where A is the cross-section of the illuminated area, $I_0 = P_0/A$ is the incident intensity, $\Delta N = [N_i - (g_i/g_k)N_k]$ is the difference of the population densities, and $\sigma_{ik}(\nu)$

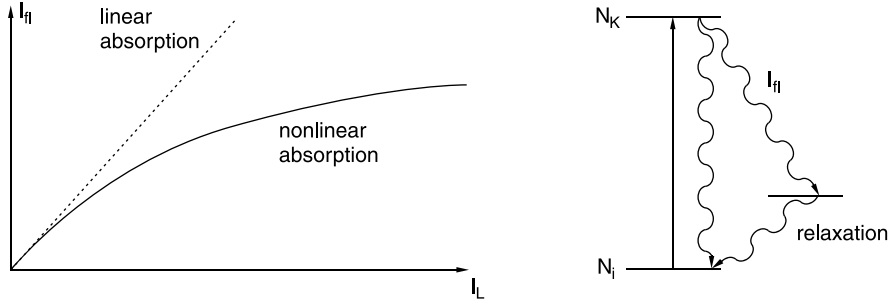


Fig. 2.1 Fluorescence intensity $I_F(I_L)$ as a function of incident laser intensity for linear and nonlinear absorption

is the absorption cross section per molecule at the light frequency $\nu = \omega/2\pi$, see (5.2) in Vol. 1.

For sufficiently low incident intensities I_0 , the absorption coefficient α is independent of I_0 (this implies that the population difference ΔN is not dependent on I_0 !), and the absorbed power dP is linearly dependent on the incident power P_0 . Integration of (2.1a) gives Beer's law of *linear absorption*:

$$P = P_0 e^{-\alpha z} = P_0 e^{-\sigma \Delta N z}. \quad (2.1b)$$

When the absorption is measured through the fluorescence intensity I_F emitted from the upper level $|k\rangle$, which is proportional to the absorbed power, we obtain the linear curve in Fig. 2.1. As the intensity of the incident radiation increases, the population N_i in the absorbing level $|i\rangle$ will be depleted when the absorption rate becomes faster than the relaxation processes that can refill it. Therefore, the absorption decreases and the curve $I_F(I_0)$ in Fig. 2.1 deviates from the straight curve until it reaches a constant value (saturation). We must then generalize (2.1a) to

$$dP = -P_0 \cdot \alpha(P_0) dz = -P_0 \sigma_{ik} \Delta N(P_0) dz \quad (2.1c)$$

where the population difference ΔN and therefore the absorption coefficient α become a function of P_0 (*nonlinear absorption*).

Example 2.1 In a first approximation we can write $\alpha = \alpha_0(1 - bI)$, which gives with a cross-section A of the incident radiation

$$dP = -AI\alpha dz = -A(I\alpha_0 - \alpha_0 b I^2) dz. \quad (2.1d)$$

The first term describes the contribution from linear absorption, and the second from nonlinear quadratic absorption.

We will now consider the nonlinear absorption in more detail.

If the incident plane wave with the spectral energy density

$$\rho_\nu(\nu) = I_\nu(\nu)/c \text{ [W s}^2\text{/m}^3\text{]}$$

has the spectral width $\delta\nu_L$, the total intensity becomes

$$I = \int I_\nu(\nu) d\nu \approx I_\nu(\nu_0) \cdot \delta\nu_L. \quad (2.2)$$

Note The difference between the spectral intensity I_ν [W s m⁻²] (radiation power per m² and frequency interval $d\nu = 1 \text{ s}^{-1}$) and the total intensity I [W m⁻²].

The absorbed power is then

$$\Delta P = \Delta N dV \cdot \int I_\nu(\nu) \cdot \sigma_{ik}(\nu) d\nu. \quad (2.3)$$

For a monochromatic laser wave tuned to the center-frequency ν_0 of an absorption line, the absorbed power is:

$$\Delta P = \Delta N dV \cdot I(\nu_0) \cdot \sigma_{ik}(\nu_0) \quad (2.4)$$

where $dV = A dz$ is the volume of the absorbing medium traversed by the laser beam with cross-section A . If the spectral width $\delta\nu_L$ of the laser is larger than the width $\delta\nu_a$ of the absorption line, only that part of the spectral interval of the laser line inside the line width $\delta\nu_a$ of the absorption line is absorbed, and the absorbed power becomes:

$$\Delta P = \Delta N dV \cdot I(\nu_0) \cdot \sigma(\nu_0) \cdot \delta\nu_a/\delta\nu_L. \quad (2.5)$$

This corresponds to $n_{\text{ph}} = \Delta P/h\nu$ absorbed photons. From Vol. 1, (2.15) we can deduce

$$n_{\text{ph}} = B_{ik} \cdot \rho(\nu) \Delta N dV. \quad (2.6)$$

$B_{ik}\rho_\nu$ gives the net probability for absorbing a photon per molecule and per second within the unit volume $dV = 1 \text{ m}^3$, see Vol. 1, (2.15), (2.18).

The comparison of (2.3) and (2.6) yields the relation between the Einstein coefficient B_{ik} and the absorption cross-section σ_{ik}

$$B_{ik} = \frac{c}{h\nu} \int_{\nu=0}^{\infty} \sigma_{ik}(\nu) d\nu, \quad (2.7)$$

where the frequencies ν outside the absorption linewidth $\delta\nu_a$ do not noticeably contribute to the integral. The absorption of the incident wave causes population changes of the levels involved in the absorbing transition. This can be described by

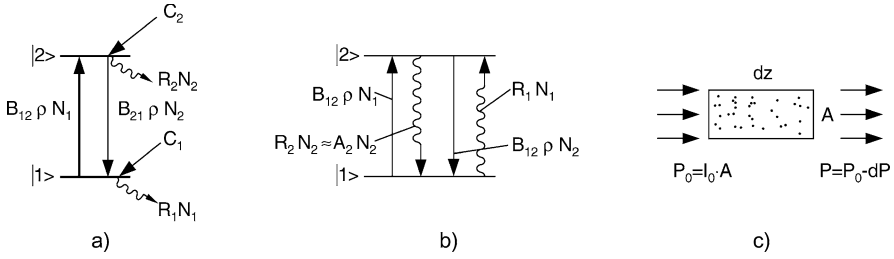


Fig. 2.2 Level diagram of an open two-level system with open relaxation channels into other levels and population paths from outside the system (a), a closed system (b), and schematic illustration of absorption (c)

the rate equations for the population densities N_1 , N_2 of the nondegenerate levels $|1\rangle$ and $|2\rangle$ with $g_1 = g_2 = 1$ (Fig. 2.2):

$$\frac{dN_1}{dt} = B_{12}\rho_v(N_2 - N_1) - R_1 N_1 + C_1, \quad (2.8a)$$

$$\frac{dN_2}{dt} = B_{12}\rho_v(N_1 - N_2) - R_2 N_2 + C_2, \quad (2.8b)$$

where $R_i N_i$ represents the total relaxation rate (including spontaneous emission) that depopulates the level $|i\rangle$ and

$$C_i = \sum_k R_{ki} N_k + D_i, \quad (2.8c)$$

takes care of all relaxation paths from other levels $|k\rangle$ that contribute to the repopulation of level $|i\rangle$ and also of the net diffusion rate D_i of molecules in level $|i\rangle$ into the excitation volume dV . We call the system described by (2.8a, 2.8b) an *open two-level system* because optical pumping occurs only between the two levels $|1\rangle$ and $|2\rangle$, which, however, may decay into other levels. That is, channels are open for transitions out of the system and for the population of the system from outside.

If the quantities C_i are not noticeably changed by the radiation field, we obtain from (2.8a–2.8c) under stationary conditions ($dN/dt = 0$) the unsaturated population difference for $\rho = 0$

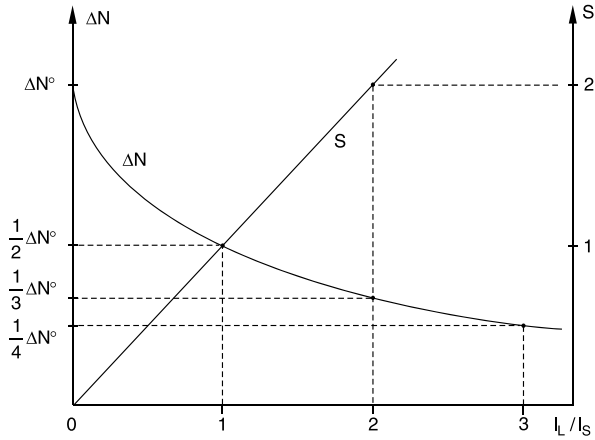
$$\Delta N^0 = \Delta N(\rho = 0) = N_2^0 - N_1^0 = \frac{C_2 R_1 - C_1 R_2}{R_1 R_2}. \quad (2.9)$$

Note that $N_1^0 > N_2^0$ and therefore $\Delta N^0 < 0$.

For the saturated population difference ($\rho \neq 0$):

$$\Delta N = \frac{\Delta N^0}{1 + B_{12}\rho_v(1/R_1 + 1/R_2)} = \frac{\Delta N^0}{1 + S}, \quad (2.10)$$

Fig. 2.3 Population difference ΔN and saturation parameter S as a function of incident laser intensity I_L



where the *saturation parameter*

$$S = \frac{B_{12}\rho_\nu}{R^*} = \frac{B_{12}I_\nu/c}{R^*} = \frac{B_{12}I}{c \cdot R_1 R_2},$$

with

$$R^* = \frac{R_1 R_2}{R_1 + R_2}, \quad (2.11)$$

gives the ratio of the induced transition probability $B_{12}\rho$ to the “mean” relaxation probability R^* . For $S \ll 1$ the homogeneous width of the absorption line is $\delta\nu_a = R_1 + R_2$ and therefore the absorbed intensity is $\Delta I = \Delta I_\nu(R_1 + R_2)$.

For $S \ll 1$, (2.10) can be written as

$$\Delta N \approx \Delta N^0(1 - S). \quad (2.12)$$

The spectral intensity $I_\nu = c \cdot R^*/B_{12} = I_s(\nu)$ at which the saturation parameter S becomes $S = 1$ is called the *saturation intensity*. The total saturation intensity is $I_s = \int I_s(\nu) d\nu \approx I_s(\nu_L) \delta\nu_L$. From (2.10) we derive that for $S = 1$ the population-density difference ΔN decreases to one half of its unsaturated value ΔN^0 (Fig. 2.3). The saturation power P_s is $P_s = I_s A$, where A is the cross section of the laser beam at the absorbing molecular sample.

Taking into account saturation, the power decrease of the incident light wave along the length dz of the absorption path is for $\delta\nu_L < \delta\nu_a$, according to (2.1a–2.1c and 2.10)

$$dP = -A \cdot I \cdot \sigma_{12} \frac{\Delta N^0}{1 + S} dz. \quad (2.13)$$

In case of incoherent light sources, such as spectral lamps, the intensity I_ν is so small that $S \ll 1$. We can then approximate (2.13) by

$$dP = -P\sigma_{12}\Delta N^0 dz, \quad (2.14)$$

where the unsaturated population difference as given by (2.9) is independent of the intensity I , and the absorbed power is proportional to the incident power (linear absorption), i.e., the relative absorbed power dP/P is constant.

Higher incident intensities I_ν are achievable with lasers, where $S \ll 1$ may be no longer valid and (2.13) instead of (2.14) has to be used. Because of the decreasing population difference the absorbed power increases less than linearly with increasing incident intensity (Fig. 2.1). The decreasing relative absorption dP/P with increasing intensity I can readily be demonstrated when the absorbed power as a function of the incident intensity is measured via the laser-induced fluorescence. If the depopulation of the absorbing level $|1\rangle$ by absorption of laser photons becomes a noticeable fraction of the repopulation rate (Fig. 2.3), the population N_1 decreases and the laser-induced fluorescence intensity increases less than linearly with the incident laser intensity I_L .

With the Rabi flopping frequency

$$\Omega_R = D_{ik} E_0 / \hbar$$

which depends on the transition dipole matrix element D_{ik} and the electric field amplitude E_0 of the incident wave (see Vol. 1, (2.90)), we can relate the saturation parameter S for homogeneous line broadening (see Vol. 1, Sect. 3.1) with a line width $\gamma = \gamma_1 + \gamma_2 = R_1 + R_2$ to the Rabi flopping frequency by

$$S_{12} = \Omega_R^2 / (R^* \cdot \gamma) = \Omega_R^2 / (R_1 R_2). \quad (2.15)$$

Using the relations (2.30, 2.78 and 2.90) from Vol. 1 with the homogeneous spectral width $\delta\omega_a = 2\pi\delta\nu_a = \gamma = \gamma_1 + \gamma_2 = R_1 + R_2$ (see Vol. 1, Sect. 3.1.2) and the Rabi frequency Ω_{12} we obtain from (2.11)

$$S = \frac{\Omega_{12}^2}{R^* \gamma} = \frac{\Omega_{12}^2}{\gamma_1 \gamma_2}, \quad \text{for } R_1 = \gamma_1, \quad R_2 = \gamma_2. \quad (2.16)$$

This demonstrates that the saturation parameter can also be expressed as the square of the ratio $\Omega_{12}/\sqrt{R_1 \cdot R_2}$ of the Rabi frequency Ω_{12} at resonance ($\omega = \omega_{12}$) and the geometric mean of the relaxation rates of $|1\rangle$ and $|2\rangle$. In other words, when the atoms are exposed to light with intensity $I = I_s$, their Rabi frequency is $\Omega_{12} = \sqrt{R_1 \cdot R_2}$.

The saturation parameter defined by (2.11) for the open two-level system is more general than that defined in Vol. 1, (3.67d) for a closed two-level system. The difference lies in the definition of the mean relaxation probability, which is $R = (R_1 + R_2)/2$ in the closed system but $R^* = R_1 R_2 / (R_1 + R_2)$ in the open system. We can close our open system defined by the rate equations (2.8a–2.8c) by setting $C_1 = R_2 N_2$, $C_2 = R_1 N_1$, and $N_1 + N_2 = N = \text{const.}$ (see Fig. 2.2b). The rate equations then become identical to Vol. 1, (3.66) and R^* converts to R .

Regarding the saturation of the absorbing-level population N_1 , there exists an important difference between a closed and an open two-level system. For the closed two-level system the stationary population density N_1 of the absorbing level $|1\rangle$ is,

according to (2.8a–2.8c) and Vol. 1, (3.67) with $C_1 = R_2 N_2$, $C_2 = R_1 N_1$, $N_1 + N_2 = N = \text{const.}$:

$$N_1 = \frac{B_{12}I/c + R_2}{2B_{12}I_v/c + R_1 + R_2} N, \quad \text{with } N = N_1 + N_2. \quad (2.17a)$$

N_1 can never drop below $N/2$ because

$$N_1 \geq \lim_{I \rightarrow \infty} N_1 = N/2 \rightarrow N_1 \geq N_2.$$

For our open system, however, we obtain from (2.8a–2.8c)

$$N_1 = \frac{(C_1 + C_2)B_{12}I_v/c + R_2 C_1}{(R_1 + R_2)B_{12}I_v/c + R_1 R_2} N. \quad (2.17b)$$

For large intensities I_v ($S \gg 1$), the population density $N_1(I)$ approaches the limit

$$N_1(S \rightarrow \infty) = \frac{C_1 + C_2}{R_1 + R_2} N. \quad (2.17c)$$

If the repopulation rates C_1 , C_2 are small compared to the depopulation rates R_1 , R_2 the saturated population density N_1 may become quite small.

This case applies, for instance, to the saturation of molecular transitions in a molecular beam, where collisions are generally negligible. The excited level $|2\rangle$ decays by spontaneous emission at the rate $N_2 A_2$ into many other rotational–vibrational levels $|m\rangle \neq |1\rangle$, and only a small fraction $N_2 A_{21}$ comes back to the level $|1\rangle$. The only repopulation mechanisms of level $|1\rangle$ are the diffusion of molecules into the excitation volume and the radiative decay rate $N_2 A_{21}$.

For $E_2 \gg kT$, the upper level $|2\rangle$ can be populated only by optical pumping. If $|1\rangle$ is the ground state, its “lifetime” is given by the transit time $t_T = d/v$ through the excitation region of length d . We therefore have to replace in (2.8a–2.8c): $C_1 = D_1 + N_2 A_{21}$, $D_2 = 0$, $R_1 = 1/t_T$, $R_2 = A_2 + 1/t_T$, and find

$$N_1 = \frac{D_1(B_{12}\rho + A_2 + 1/t_T)}{B_{12}\rho(A_2 - A_{21} + 2/t_T) + 1/t_T^2} N. \quad (2.18a)$$

Without the laser excitation ($\rho = 0$, $A_2 = A_{21} = 0$), we obtain $N_1^0 = D_1 t_T$. This is the stationary population due to the diffusion of molecules into the excitation region. For large laser intensities, (2.18a) yields

$$\lim_{I \rightarrow \infty} N_1 = \frac{D_1}{A_2 - A_{21} + 2/t_T}. \quad (2.18b)$$

Example 2.2 For $d = 1$ mm, $v = 5 \times 10^4$ cm/s $\rightarrow t_T = 2 \times 10^{-6}$ s. With $D_1 = 10^{14}$ s $^{-1}$ cm $^{-3}$ we have the stationary population density $N_1^0 = 2 \times 10^8$ cm $^{-3}$. With typical figures of $A_2 = 10^8$ s $^{-1}$, $A_{21} = 10^7$ s $^{-1}$ we obtain for the completely saturated population density $N_1 \approx 10^6$ cm $^{-3}$. The saturated population N_1 has therefore decreased to 0.5 % of its unsaturated value N_1^0 .

We shall now briefly illustrate for two different situations at which intensities the saturation becomes noticeable:

- (a) The bandwidth $\delta\nu_L$ of the cw laser is larger than the spectral width $\delta\nu_a$ of the absorbing transition. In this case, we get the same results both for homogeneous and inhomogeneous line broadening. The total saturation intensity $I_s = c\rho_s(\nu)\delta\nu_L$ is then according to (2.11)

$$I_s = \int I_s(\nu) d\nu \approx \frac{R^*c}{B_{12}}\delta\nu_L \text{ [W/m}^2\text{]}. \quad (2.19a)$$

Example 2.3 Saturation of a molecular transition in a molecular beam by a broadband cw laser with $\delta\nu_L = 3 \times 10^9$ s $^{-1}$ ($\hat{=} 0.1$ cm $^{-1}$): With $R_1 = 1/t_T$, $R_2 = A_2 + 1/t_T$, we obtain with $B_{12} = (c^3/8\pi h\nu^3)A_{21}$ the saturation intensity

$$I_s(\delta\nu_L) = \frac{(A_2 + 1/t_T)8\pi h\nu^3 \cdot \delta\nu_L}{(t_TA_2 + 2)A_{21}c^2} \text{ [W/m}^2\text{]}. \quad (2.19b)$$

With the values of our previous example $A_2 = 10^8$ s $^{-1}$, $t_T = 2 \times 10^{-6}$ s, $\nu = 5 \times 10^{14}$ s $^{-1}$, $A_{21} = 10^7$ s $^{-1}$, and $\delta\nu_L = 3 \times 10^9$ s $^{-1}$, which gives

$$I_s \approx 3 \times 10^3 \text{ W/m}^2.$$

If the laser beam is focused to a cross section of $A = 1$ mm 2 , a laser power of 3 mW is sufficient for our example to reach the value $S = 1$ of the saturation parameter.

If the laser bandwidth $\delta\nu_L$ matches the homogeneous width $\gamma/2\pi$ of the absorption line, we find with $\gamma = A_2 + 2/t_T$ from (2.19b) the saturation intensity

$$I_s = \frac{4h\nu^3}{T A_{21}c^2}(A_2 + 1/t_T) \approx 100 \text{ W/m}^2 = 100 \text{ }\mu\text{W/mm}^2. \quad (2.19c)$$

If the laser beam is focussed to a cross section $10 \times 10 \text{ }\mu\text{m}^2$ the saturation power decreases to $P_s = 10$ nW!

- (b) The second case deals with a cw single-mode laser with frequency $\nu = \nu_0$ tuned to the center frequency ν_0 of a homogeneously broadened atomic resonance transition. If spontaneous emission into the ground state is the only relaxation process of the upper level, the relaxation rate is $R^* = A_{21}/2$ for $S = 1$, the saturation-broadened linewidth is $\delta\nu_a = \sqrt{2}A_{21}/2\pi$, and the saturation intensity is, according to (2.11) and Vol. 1, (2.22)

$$I_s = c\rho_s\delta\nu_a = \frac{cR^*A_{21}}{\sqrt{2}\pi B_{12}} = \frac{2\sqrt{2}h\nu A_{21}}{\lambda^2}. \quad (2.20)$$

The same result could have been obtained from Vol. 1, (3.67f) $I_s = h\nu A_{21}/2\sigma_{12}$ with

$$\int \sigma_{12} d\nu \sim \sigma(\nu_0)\delta\nu_a = (h\nu/c)B_{12} = (c^2/8\pi\nu^2)A_{21}, \quad (2.21a)$$

which yields without saturation broadening

$$\sigma(\nu_0) \sim c^2/4\nu^2 = (\lambda/2)^2, \quad \text{and} \quad I_s = \frac{2h\nu A_{21}}{\lambda^2}. \quad (2.21b)$$

For $A_{21} = 10^8 \text{ s}^{-1}$ the relaxation due to diffusion out of the excitation volume can be neglected. At sufficiently low pressures the collision-induced transition probability is small compared to A_{21} .

Example 2.4 $\lambda = 500 \text{ nm} \rightarrow \nu = 6 \times 10^{14} \text{ s}^{-1}$, $A_{21} = 10^8 \text{ s}^{-1} \rightarrow I_s \approx 380 \text{ W/m}^2$. Focusing the beam to a focal area of 1 mm^2 means a saturation power of only $265 \text{ }\mu\text{W}$! With the value $A_{21} = 10^7 \text{ s}^{-1}$ of Example 2.3, the saturation intensity drops to 38 W/m^2 . Focussing to $10 \times 10 \text{ }\mu\text{m}^2$ reduces the saturation power to 3.8 nW .

If collision broadening is essential, the linewidth increases and the saturation intensity increases roughly proportionally to the homogeneous linewidth. If pulsed lasers are used, the saturation peak powers are much higher because the system does generally not reach the stationary conditions. For the optical pumping time the laser pulse duration T_L often is the limiting time interval. Only for long laser pulses (e.g., copper-vapor laser-pumped dye lasers) the transit time of the molecules through the laser beam may be shorter than T_L .

2.2 Saturation of Inhomogeneous Line Profiles

In Vol. 1, Sect. 3.6 we saw that the saturation of *homogeneously broadened* transitions with Lorentzian line profiles results again in a Lorentzian profile with the

halfwidth

$$\Delta\omega_s = \Delta\omega_0\sqrt{1 + S_0}, \quad S_0 = S(\omega_0), \quad (2.22)$$

which is increased by the factor $(1 + S_0)^{1/2}$ compared to the unsaturated halfwidth $\Delta\omega_0$. The saturation broadening is due to the fact that the absorption coefficient

$$\alpha(\omega) = \frac{\alpha_0(\omega)}{1 + S(\omega)}$$

decreases by the factor $[1 + S(\omega)]^{-1}$, whereas the saturation parameter $S(\omega)$ itself has a Lorentzian line profile and the saturation is stronger at the line center than in the line wings (Vol. 1, Fig. 3.24).

We will now discuss saturation of inhomogeneous line profiles. As an example we treat Doppler-broadened transitions, which represent the most important case in saturation spectroscopy.

2.2.1 Hole Burning

When a monochromatic light wave

$$E = E_0 \cos(\omega t - kz), \quad \text{with } k = k_z,$$

passes through a gaseous sample of molecules with a Maxwell–Boltzmann velocity distribution, only those molecules that move with such velocities \mathbf{v} that the Doppler-shifted laser frequency in the frame of the moving molecule $\omega' = \omega - \mathbf{k} \cdot \mathbf{v}$ with $\mathbf{k} \cdot \mathbf{v} = kv_z$ falls within the homogeneous linewidth γ around the center absorption frequency ω_0 of a molecule at rest, i.e., $\omega' = \omega_0 \pm \gamma$, can significantly contribute to the absorption. The absorption cross section for a molecule with the velocity component v_z on a transition $|1\rangle \rightarrow |2\rangle$ is without saturation ($S = 0$)

$$\sigma_{12}(\omega, v_z) = \sigma_0 \frac{(\gamma/2)^2}{(\omega - \omega_0 - kv_z)^2 + (\gamma/2)^2}, \quad (2.23)$$

where $\sigma_0 = \sigma(\omega = \omega_0 + kv_z)$ is the maximum absorption cross section at the line center of the Doppler-shifted molecular transition.

Due to saturation, the population density $N_1(v_z)dv_z$ decreases within the velocity interval $dv_z = \gamma/k$, while the population density $N_2(v_z)dv_z$ of the upper level $|2\rangle$ increases correspondingly (Fig. 2.4a). From (2.10) and Vol. 1, (3.72) we obtain for $S \ll 1$

$$N_i^0 - N_i = \frac{\Delta N_i^0}{1 + S} \approx \Delta N_i^0 (1 - S).$$

The saturation parameter S is

$$S(\omega) = S_0 \cdot \frac{(\gamma/2)^2}{(\omega - \omega_0)^2 + (\gamma/2)^2}.$$

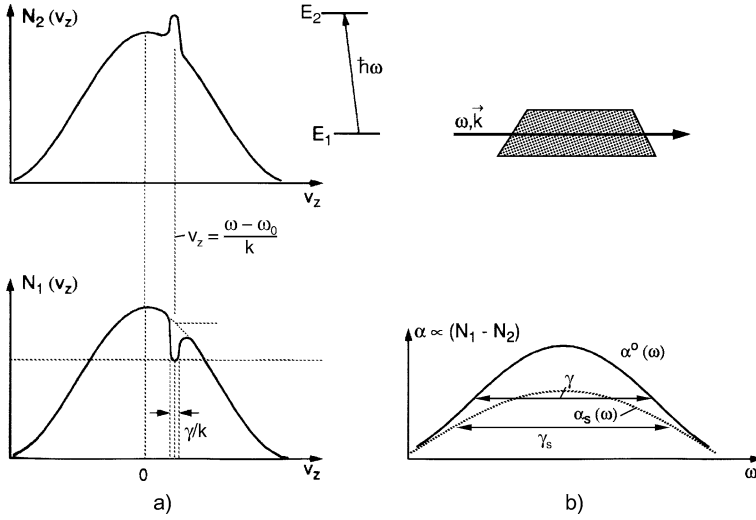


Fig. 2.4 Velocity-selective saturation of a Doppler-broadened transition: **(a)** the Bennett hole in the lower- and the Bennett peak in the upper-state population distribution $N_i(v_z)$. **(b)** Saturated absorption profile when the saturating laser is tuned across the Doppler-profile of a molecular transition (*dashed curve*)

With $\gamma_s = \gamma \cdot \sqrt{1 + S}$ and $\omega_0 \rightarrow \omega_0 + kv_z$ one obtains

$$N_1(\omega, v_z) = N_1^0(v_z) - \frac{\Delta N^0}{\gamma_1 \tau} \left[\frac{S_0(\gamma/2)^2}{(\omega - \omega_0 - kv_z)^2 + (\gamma_s/2)^2} \right], \quad (2.24a)$$

$$N_2(\omega, v_z) = N_2^0(v_z) + \frac{\Delta N^0}{\gamma_2 \tau} \left[\frac{S_0(\gamma/2)^2}{(\omega - \omega_0 - kv_z)^2 + (\gamma_s/2)^2} \right], \quad (2.24b)$$

where $\gamma = \gamma_1 + \gamma_2$ denotes the homogeneous width of the transition and $\gamma_s = \gamma \sqrt{1 + S_0}$. The quantity

$$\tau = \frac{1}{\gamma_1} + \frac{1}{\gamma_2} = \frac{\gamma}{\gamma_1 \cdot \gamma_2}, \quad (2.24c)$$

is called the *longitudinal relaxation time*, while

$$T = \frac{1}{\gamma_1 + \gamma_2} = \frac{1}{\gamma} \quad (2.24d)$$

is the *transverse relaxation time*.

Note that for $\gamma_1 \neq \gamma_2$ the depth of the hole in $N_1(v_z)$ and the heights of the peak in $N_2(v_z)$ are different.

Subtracting (2.24b) from (2.24a) yields for the saturated population difference

$$\Delta N(\omega_s, v_z) = \Delta N^0(v_z) \left[1 - \frac{S_0(\gamma/2)^2}{(\omega - \omega_0 - kv_z)^2 + (\gamma_s/2)^2} \right]. \quad (2.24e)$$

The velocity-selective minimum in the velocity distribution $\Delta N(v_z)$ at $v_z = (\omega - \omega_0)/k$, which is often called a *Bennet hole* [202], has the homogeneous width (according to Vol. 1, Sect. 3.6)

$$\gamma_s = \gamma \sqrt{1 + S_0},$$

and a depth at the hole center at $\omega = \omega_0 + kv_z$ of

$$\Delta N^0(v_z) - \Delta N(v_z) = \Delta N^0(v_z) \frac{S_0}{1 + S_0}. \quad (2.25)$$

For $S_0 = 1$ the hole depth amounts to 50 % of the unsaturated population difference. Molecules with velocity components in the interval v_z to $v_z + dv_z$ give the contribution

$$d\alpha(\omega, v_z) dv_z = \Delta N(v_z) \sigma(\omega, v_z) dv_z, \quad (2.26)$$

to the absorption coefficient $\alpha(\omega, v_z)$. The total absorption coefficient caused by all molecules in the absorbing level is then

$$\alpha(\omega) = \int \Delta N(v_z) \sigma_{12}(\omega, v_z) dv_z. \quad (2.27)$$

Inserting $\Delta N(v_z)$ from (2.24a–2.24e), $\sigma(\omega, v_z)$ from (2.23) and $\Delta N^0(v_z)$ from Vol. 1, (3.40) yields

$$\alpha(\omega) = \frac{\Delta N \sigma_0}{v_p \sqrt{\pi}} \int \frac{e^{-(v_z/v_p)^2} dv_z}{(\omega - \omega_0 - kv_z)^2 + (\gamma_s/2)^2}, \quad (2.28)$$

with the most probable velocity $v_p = (2k_B T/m)^{1/2}$ and the total saturated population difference $\Delta N = \int \Delta N(v_z) dv_z$. Despite the saturation, one obtains again a Voigt profile for $\alpha(\omega)$, similarly to Vol. 1, (3.46). The only difference is the saturation-broadened homogeneous linewidth γ_s in (2.28) instead of γ in Vol. 1, (3.33) (Fig. 2.4b).

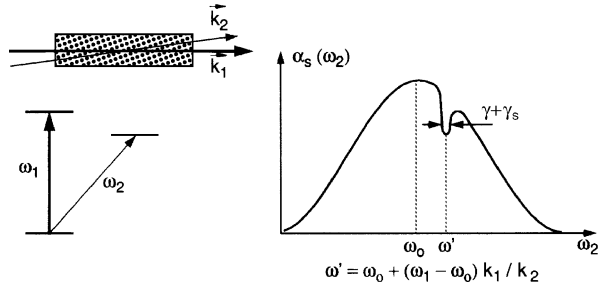
Since for $S_0 < 1$ the Doppler width is generally large compared to the homogeneous width γ_s , the nominator in (2.28) at a given frequency ω does not vary much within the interval $\Delta v_z = \gamma_s/k$, where the integrand contributes significantly to $\alpha(\omega)$. We therefore can take the factor $\exp[-(v_z/v_p)^2]$ outside the integral. The residual integrals can be solved analytically and one obtains with $v_z = (\omega - \omega_0)/k$ and Vol. 1, (3.44) the saturated absorption coefficient

$$\alpha_s(\omega) = \frac{\alpha^0(\omega_0)}{\sqrt{1 + S_0}} \exp \left\{ - \left[\frac{\omega - \omega_0}{0.6 \delta \omega_D} \right]^2 \right\}, \quad (2.29)$$

with the unsaturated absorption coefficient

$$\alpha^0(\omega_0) = \Delta N_0 \frac{\sigma_0 \gamma c \sqrt{\pi}}{v_p \omega_0},$$

Fig. 2.5 Dip in the Doppler-broadened absorption profile $\alpha(\omega)$ burned by a strong pump laser at $\omega_p = \omega_1$ and detected by a weak probe laser at $\omega' = \omega_0 \pm (\omega_1 - \omega_0)k_1/k_2$



and the Doppler width

$$\delta\omega_D = \frac{\omega_0}{c} \sqrt{\frac{8kT \ln 2}{m}},$$

Eq. (2.29) illustrates a remarkable result: *Although at each frequency ω the monochromatic laser burns a Bennet hole into the velocity distribution $N_1(v_z)$, this hole cannot be detected just by tuning the laser through the absorption profile.* The absorption coefficient

$$\alpha(\omega) = \frac{\alpha^0(\omega)}{\sqrt{1 + S_0}}, \quad (2.30)$$

of the inhomogeneous profile still shows a Voigt profile *without any hole* but is reduced by the constant factor $(1 + S_0)^{-1/2}$, which is independent of ω (Fig. 2.4b).

Note The difference to the homogeneous absorption profile where $\alpha(\omega)$ is reduced by the *frequency-dependent* factor $(1 + S(\omega))^{-1}$, see Vol. 1, (3.69) and Fig. 3.23 is the fact, that for the inhomogeneous profile the reduction factor $(1 + S_0)^{-1}$ is independent of the frequency ω .

The Bennet hole can, however, be detected if *two lasers* are used:

- The saturating pump laser with the wave vector \mathbf{k}_1 , which is kept at the frequency ω_1 and which burns a hole, according to (2.24a–2.24e), into the velocity class $v_z \pm \Delta v_z/2$ with $v_z = (\omega_0 - \omega_1)/k_1$ and $\Delta v_z = \gamma/k_1$ (Fig. 2.5).
- A weak probe laser with the wave vector \mathbf{k}_2 and a frequency ω tunable across the Voigt profile. This probe laser is sufficiently weak to cause no extra saturation. The absorption coefficient for the tunable probe laser is then

$$\begin{aligned} \alpha_s(\omega_1, \omega) = & \frac{\sigma_0 \Delta N^0}{v_p \sqrt{\pi}} \int \frac{e^{-(v_z/v_p)^2}}{(\omega_0 - \omega - k_2 v_z)^2 + (\gamma/2)^2} \\ & \times \left[1 - \frac{S_0(\gamma/2)^2}{(\omega_0 - \omega_1 - k_1 v_z)^2 + (\gamma_s/2)^2} \right] dv_z. \end{aligned} \quad (2.31)$$

The integration over the velocity distribution yields analogously to (2.29)

$$\alpha_s(\omega_1, \omega) = \alpha^0(\omega) \left[1 - \frac{S_0}{\sqrt{1+S_0}} \frac{(\gamma/2)^2}{(\omega - \omega')^2 + (\Gamma_s/2)^2} \right]. \quad (2.32)$$

This is an unsaturated Doppler profile $\alpha^0(\omega)$ with a saturation dip at the probe frequency

$$\omega = \omega' = \omega_0 \pm (\omega_1 - \omega_0)k_1/k_2,$$

where the $+$ sign holds for collinear and the $-$ sign for anticollinear propagation of the pump and probe waves.

The halfwidth $\Gamma_s = \gamma + \gamma_s = \gamma[1 + (1 + S_0)^{1/2}]$ of the absorption dip at $\omega = \omega'$ equals the sum of the unsaturated homogeneous absorption width γ of the weak probe wave and that of the saturated dip (due to the strong pump). The depth of the dip at $\omega = \omega'$ is

$$\begin{aligned} \Delta\alpha(\omega') &= \alpha^0(\omega') - \alpha_s(\omega') = \alpha^0(\omega') \frac{S_0}{\sqrt{1+S_0}[(1 + \sqrt{1+S_0})]^2} \\ &\approx \frac{S_0}{4} \alpha^0(\omega'), \quad \text{for } S_0 \ll 1. \end{aligned} \quad (2.32a)$$

Note In the derivation of (2.32) we have only regarded population changes due to saturation effects. We have neglected coherence phenomena that may, for instance, result from interference between the two waves. These effects, which differ for copropagating waves from those of counterpropagating waves, have been treated in detail in [203–205]. For sufficiently small laser intensities ($S \ll 1$) they do not strongly affect the results derived above, but add finer details to the spectral structures obtained.

2.2.2 Lamb Dip

Pump and probe waves may also be generated by a single laser when the incident beam is reflected back into the absorption cell (Fig. 2.6).

The saturated population difference in such a case of equal intensities $I_1 = I_2 = I$ of the two counterpropagating waves with wavevectors $\mathbf{k}_1 = -\mathbf{k}_2$ is then

$$\begin{aligned} \Delta N(v_z) &= \Delta N^0(v_z) \\ &\times \left[1 - \frac{S_0(\gamma/2)^2}{(\omega_0 - \omega - kv_z)^2 + (\gamma_s/2)^2} - \frac{S_0(\gamma/2)^2}{(\omega_0 - \omega + kv_z)^2 + (\gamma_s/2)^2} \right], \end{aligned} \quad (2.33)$$

where $S_0 = S_0(I)$ is the saturation parameter due to one of the running waves. Because of the opposite Doppler shifts the two waves with frequency ω burn two

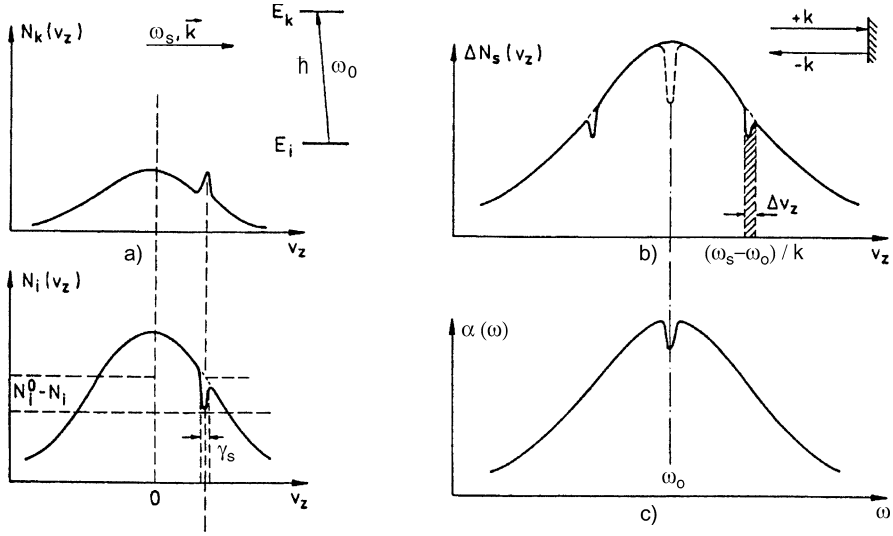


Fig. 2.6 Saturation of an inhomogeneous line profile: (a) Bennet hole and dip produced by a monochromatic running wave with $\omega \neq \omega_0$; (b) Bennet holes caused by the two counterpropagating waves for $\omega \neq \omega_0$ and for $\omega = \omega_0$ (dashed curve); (c) Lamb dip in the absorption profile $\alpha_s(\omega)$

Bennet holes at the velocity components $v_z = \pm(\omega_0 - \omega)/k$ into the population distribution $\Delta N(v_z)$ (Fig. 2.6b).

The saturated absorption coefficient then becomes

$$\alpha_s(\omega) = \int \Delta N(v_z) [\sigma(\omega_0 - \omega - kv_z) + \sigma(\omega_0 - \omega + kv_z)] dv_z. \quad (2.34)$$

Inserting (2.33 and 2.23) into (2.34) yields in the weak-field approximation ($S_0 \ll 1$) after some elaborate calculations [203] the saturated-absorption coefficient for a sample in a standing-wave field

$$\alpha_s(\omega) = \alpha^0(\omega) \left[1 - \frac{S_0}{2} \left(1 + \frac{(\gamma_s/2)^2}{(\omega - \omega_0)^2 + (\gamma_s/2)^2} \right) \right], \quad (2.35a)$$

with

$$\gamma_s = \gamma \sqrt{1 + S_0}, \quad \text{and} \quad S_0 = S_0(I, \omega_0).$$

This represents the Doppler-broadened absorption profile $\alpha^0(\omega)$ with a dip at the line center $\omega = \omega_0$ (Fig. 2.6c), which is called a *Lamb dip* after W.E. Lamb, who first explained it theoretically [206]. For $\omega = \omega_0$ the saturated absorption coefficient drops to $\alpha_s(\omega_0) = \alpha^0(\omega_0) \cdot (1 - S_0)$. The depth of the Lamb dip is $S_0 = B_{ik}I/(c\gamma_s)$, $I = I_1 = I_2$ being the intensity of one of the counterpropagating waves that form the standing wave. For $\omega_0 - \omega \gg \gamma_s$ the saturated absorption coefficient becomes $\alpha_s = \alpha_0(1 - S_0/2)$, which corresponds to the saturation by one of the two waves.

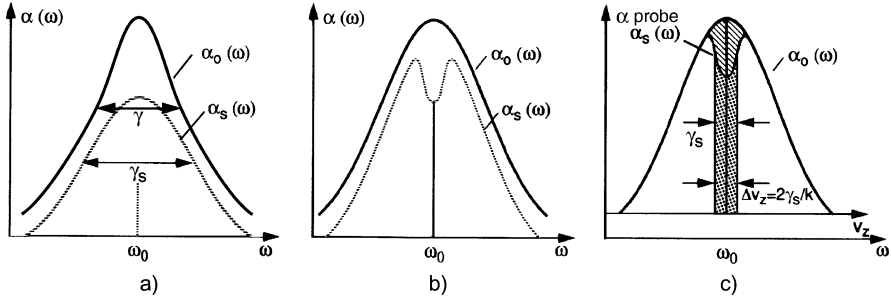


Fig. 2.7 Comparison of the saturation of a homogeneous absorption line profile (a) and an inhomogeneous profile (b) in a standing-wave field. (c) The traveling saturating wave is kept at $\omega = \omega_0$ and a weak probe wave is tuned across the line profile

The Lamb dip can be understood in a simple, conspicuous way: for $\omega \neq \omega_0$ the incident wave is absorbed by molecules with the velocity components $v_z = +(\omega - \omega_0 \mp \gamma_s/2)/k$, the reflected wave by other molecules with $v_z = -(\omega - \omega_0) \pm \gamma_s/2$. For $\omega = \omega_0$ both waves are absorbed by the same molecules with $v_z = (0 \pm \gamma_s/s)/k$, which essentially move perpendicularly to the laser beams. The intensity per molecule absorbed is now twice as large, and the saturation accordingly higher.

In Fig. 2.7 the differences in the saturation behavior of a homogeneous (Fig. 2.7a) and an inhomogeneous line profile are illustrated. For the inhomogeneous case two situations are illustrated:

- The absorbing sample is placed in a standing-wave field ($I_1 = I_2 = I$) and the frequency ω is tuned over the line profiles (Fig. 2.7b).
- A pump laser ($I = I_1$) is kept at the line center at ω_0 and a weak probe laser is tuned over the saturated line profiles (Fig. 2.7c).

In the first case (Fig. 2.7c), the saturation of the inhomogeneous line profile is $S_0 = B_{ik}I/(c\gamma_s)$ at the center of the Lamb dip and $S_0/2$ for $(\omega - \omega_0) \gg \gamma_s$. In the second case (Fig. 2.7b), the depth of the Bennett hole is $S_0/2 = B_{ik}I_1/(c\gamma_s)$.

For strong laser fields the approximation $S_0 \ll 1$ no longer holds. Instead of (2.35a, 2.35b) one obtains, neglecting coherent effects [203]:

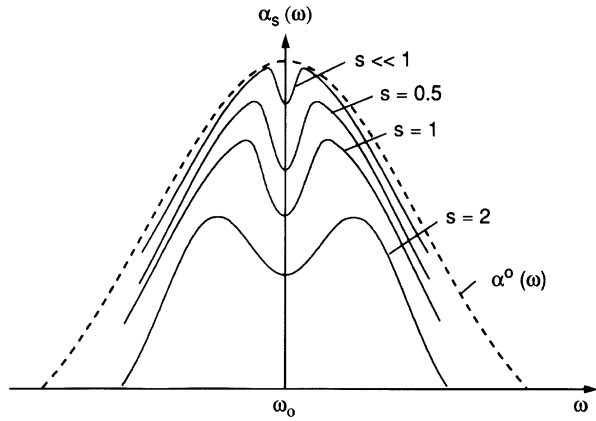
$$\alpha_s(\omega) = \alpha^0(\omega) \frac{\gamma/2}{B[1 - (\frac{2(\omega - \omega_0)}{A+B})^2]^{1/2}}, \quad (2.35b)$$

with

$$A = [(\omega - \omega_0)^2 + (\gamma/2)^2]^{1/2} \quad \text{and} \quad B = [(\omega - \omega_0)^2 + (\gamma/2)^2(1 + 2S)]^{1/2}.$$

This yields $\alpha_s(\omega_0) = \alpha^0(\omega_0)/\sqrt{1 + 2S}$ at the line center $\omega = \omega_0$, and $\alpha_s(\omega) = \alpha^0(\omega)/\sqrt{1 + S}$ for $(\omega - \omega_0) \gg \gamma$. The maximum depth of the Lamb dip is achieved

Fig. 2.8 Lamb dips for several values of the saturation parameter S_0



when

$$\frac{\alpha(\omega - \omega_0 \gg \gamma_s) - \alpha(\omega_0)}{\alpha(\omega_0)} = \frac{1}{\sqrt{1 + S_0}} - \frac{1}{\sqrt{1 + 2S_0}},$$

becomes maximum, which occurs for $S_0 \approx 1.4$. In Fig. 2.8 the saturated absorption profile is depicted for some values of S_0 .

Note The width of the Lamb dip in (2.35a) is $\delta\omega_{LD} = \gamma_s$. This corresponds, however, to the velocity interval $\Delta v_z = 2\gamma_s/k$ because the opposite Doppler shifts $\Delta\omega = (\omega_0 - \omega) = \pm kv_z$ of the two Bennett holes add when the laser frequency ω is tuned.

If the intensity of the reflected wave in Fig. 2.6 is very small ($I_2 \ll I_1$), we obtain instead of (2.35a, 2.35b) a formula similar to (2.32). However, we must replace Γ_s by $\Gamma_s^* = (\gamma + \gamma_s)/2$ since the pump and probe waves are simultaneously tuned. For $S_0 \ll 1$ the result is

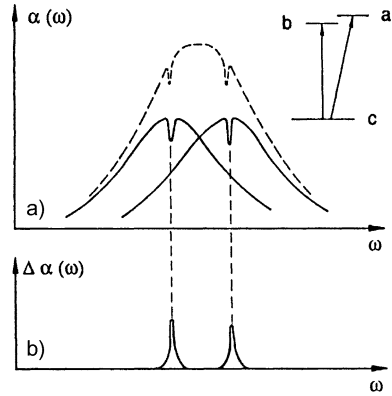
$$\alpha_s(\omega) = \alpha^0(\omega) \left[1 - \frac{S_0}{2} \frac{(\gamma_s/2)^2}{(\omega - \omega_0)^2 + (\Gamma_s^*/2)^2} \right]. \quad (2.36)$$

2.3 Saturation Spectroscopy

Saturation spectroscopy is based on the velocity-selective saturation of Doppler-broadened molecular transitions, treated in Sect. 2.2. Here the spectral resolution is no longer limited by the Doppler width but only by the much narrower width of the Lamb dip. The gain in spectral resolution is illustrated by the example of two transitions from a common lower level $|c\rangle$ to two closely spaced levels $|a\rangle$ and $|b\rangle$ (Fig. 2.9). Even when the Doppler profiles of the two transitions completely overlap, their narrow Lamb dips can clearly be separated, as long as $\Delta\omega = \omega_{ca} - \omega_{cb} > 2\gamma_s$.

Saturation spectroscopy is therefore often called *Lamb-dip spectroscopy*.

Fig. 2.9 Spectral resolution of the Lamb dips of two transitions with overlapping Doppler profiles: (a) direct measurement of Doppler-profiles and Lamb dips; (b) lock-in detection of $(\alpha^0(\omega) - \alpha_s(\omega))$



2.3.1 Experimental Schemes

A possible experimental realization of saturation spectroscopy is illustrated in Fig. 2.10. The output beam from a tunable laser is split by the beam splitter BS into a strong pump beam with the intensity I_1 and a weak probe beam with intensity $I_2 \ll I_1$, which pass through the absorbing sample in opposite directions. When the transmitted probe-beam intensity $I_{t2}(\omega)$ is measured as a function of the laser frequency ω , the detection signal $DS(\omega) \propto I_2 - I_{t2}$ shows the Doppler-broadened absorption profiles with “Lamb peaks” at their centers, because the saturated absorption shows Lamb dips at the centers of the Doppler-broadened absorption lines.

The Doppler-broadened background can be eliminated if the pump beam is chopped and the transmitted probe intensity is monitored through a lock-in amplifier that is tuned to the chopping frequency. According to (2.36), we obtain for a sufficiently weak probe intensity the Doppler-free absorption profile

$$\alpha_0 - \alpha_s = \frac{\alpha_0 S_0}{2} \frac{(\gamma_s/2)^2}{(\omega - \omega_0)^2 + (\Gamma_s^*/2)^2}. \quad (2.37)$$

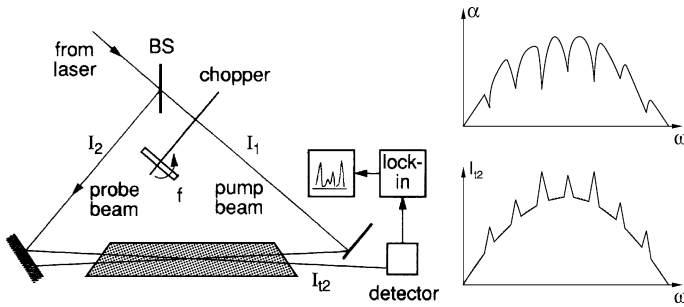
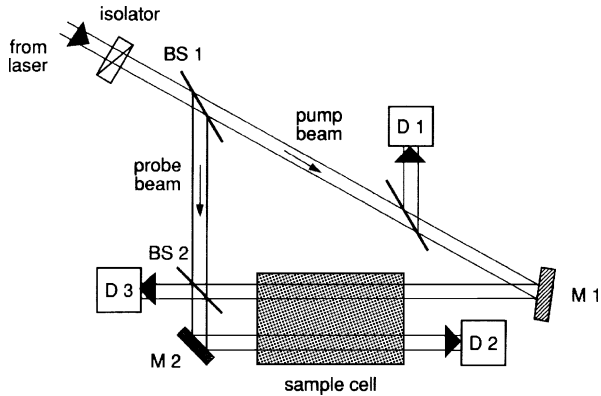


Fig. 2.10 Experimental setup for saturation spectroscopy where the transmitted probe intensity $I_{t2}(\omega)$ is monitored

Fig. 2.11 Sensitive version of saturation spectroscopy. The probe is split by BS2 into two parallel beams, which pass through a pumped and an unpumped region, respectively. Pump and probe beams are strictly antiparallel. A Faraday isolator prevents feedback of the probe beam into the laser



To enhance the sensitivity, the probe beam can again be split into two parts. One beam passes the region of the sample that is saturated by the pump beam, and the other passes the sample cell at an unsaturated region (Fig. 2.11). The difference between the two probe-beam outputs monitored with the detectors D1 and D2 yields the saturation signal if this difference has been set to zero with the pump beam off. The pump-beam intensity measured by D3 can be used for normalization of the saturation signal. Figure 2.12 shows as an example the saturation spectrum of a mixture of different cesium isotopes contained in a glass cell heated to about 100 °C [207]. The hyperfine structure and the isotope shifts of the different isotopes can be derived from these measurements with high accuracy. The small crossing angle α [rad] of the two beams in Fig. 2.10 results in a residual Doppler width $\delta\omega_1 = \Delta\omega_D\alpha$. If the pump and probe beams are strictly anticollinear ($\alpha = 0$) the probe beam is coupled back into the laser, resulting in laser instabilities. This can be prevented by an optical isolator, such as a Faraday isolator [208], which turns the plane of polarization by 90° and suppresses the reflected beam by a polarizer (Fig. 2.11).

Instead of measuring the *attenuation* of the probe beam, the absorption can also be monitored by the laser-induced *fluorescence*, which is proportional to the ab-

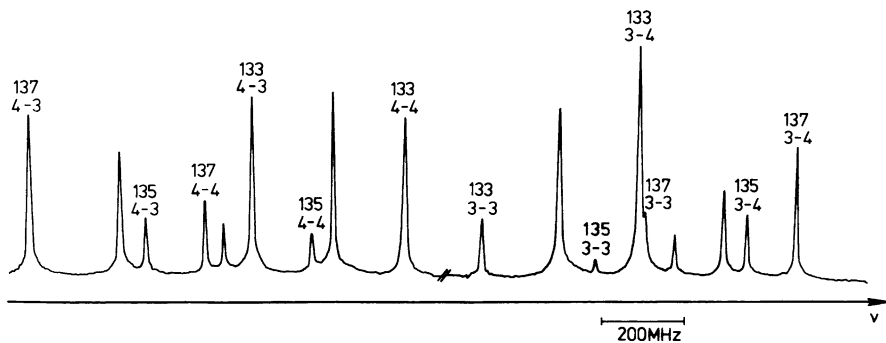
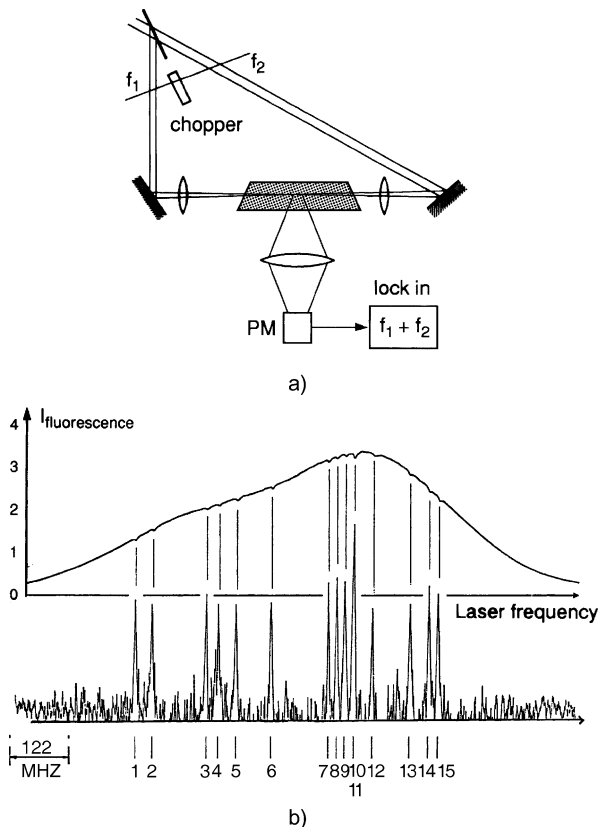


Fig. 2.12 Saturation spectrum of all hyperfine components of the $6^2S_{1/2} \rightarrow 7^2P$ transition at $\lambda = 459.3$ nm in a mixture of isotopes ^{133}Cs , ^{135}Cs , and ^{137}Cs [207]

Fig. 2.13 Intermodulated fluorescence method for saturation spectroscopy at small densities of the sample molecules: (a) experimental arrangement; (b) hyperfine spectrum of the $(v'' = 1, J'' = 98) \rightarrow (v' = 58, J' = 99)$ line in the $X^1\Sigma_g \rightarrow ^3\Pi_{0u}$ system of I_2 at $\lambda = 514.5$ nm, monitored at the chopping frequency f_1 of the pump beam (*upper spectrum with the Lamb dips*) and at $(f_1 + f_2)$ (*lower spectrum*) [211]



sorbed laser power. This technique is, in particular, advantageous when the density of the absorbing molecules is low and the absorption accordingly small. The change in the attenuation of the probe beam is then difficult to detect and the small Lamb dips may be nearly buried under the noise of the Doppler-broadened background. Sorensen and Schawlow [209, 210] have demonstrated a very sensitive *intermodulated fluorescence technique*, where the pump beam and the probe beam are chopped at two different frequencies f_1 and f_2 (Fig. 2.13a). Assume the intensities of the two beams to be $I_1 = I_{10}(1 + \cos \Omega_1 t)$ and $I_2 = I_{20}(1 + \cos \Omega_2 t)$ with $\Omega_i = 2\pi f_i$. The intensity of the laser-induced fluorescence is then

$$I_{\text{FI}} = C \Delta N_s (I_1 + I_2), \quad (2.38)$$

where ΔN_s is the difference between the saturated population densities of the absorbing and upper levels, and the constant C includes the transition probability and the collection efficiency of the fluorescence detector. According to (2.33), we obtain at the center of an absorption line

$$\Delta N_s = \Delta N^0 [1 - a(I_1 + I_2)].$$

Inserting this into (2.38) gives

$$I_{\text{F}} = C[\Delta N^0(I_1 + I_2) - a\Delta N^0(I_1 + I_2)^2]. \quad (2.39)$$

The quadratic expression $(I_1 + I_2)^2$ contains the frequency-dependent term

$$I_{10}I_{20} \cos \Omega_1 t \cdot \cos \Omega_2 t = \frac{1}{2} I_{10}I_{20} [\cos(\Omega_1 + \Omega_2)t + \cos(\Omega_1 - \Omega_2)t],$$

which reveals that the fluorescence intensity contains linear terms, modulated at the chopping frequencies f_1 and f_2 , respectively, and quadratic terms with the modulation frequencies $(f_1 + f_2)$ and $(f_1 - f_2)$, respectively. While the linear terms represent the normal laser-induced fluorescence with a Doppler-broadened excitation line profile, the quadratic ones describe the saturation effect because they depend on the decrease of the population density ΔN ($v_z = 0$) from the simultaneous interaction of the molecules with both fields. When the fluorescence is monitored through a lock-in amplifier tuned to the sum frequency $f_1 + f_2$, the linear background is suppressed and only the saturation signals are detected. This is demonstrated by Fig. 2.13b, which shows the 15 hyperfine components of the rotational line ($v'' - 1$, $J'' = 98$) ($v' = 58$, $J' = 99$) in the $X^1\Sigma_g^+ \rightarrow B^3\Pi_{0u}$ transition of the iodine molecule I_2 [210, 211]. The two laser beams were chopped by a rotating disc with two rows of a different number of holes, which interrupted the beams at $f_1 = 600 \text{ s}^{-1}$ and $f_2 = 900 \text{ s}^{-1}$. The upper spectrum was monitored at the chopping frequency f_1 of the pump beam. The Doppler-broadened background caused by the linear terms in (2.39) and the Lamb dips both show a modulation at the frequency f_1 and are therefore recorded simultaneously. The center frequencies of the hyperfine structure (hfs) components, however, can be obtained more accurately from the intermodulated fluorescence spectrum (lower spectrum), which was monitored at the sum frequency $(f_1 + f_2)$ where the linear background is suppressed. This technique has found wide applications for sub-Doppler modulation spectroscopy of molecules and radicals at low pressures [212–214].

Example 2.5 The linewidth of the Lamb dips of the I_2 hfs components can be estimated as follows. The spontaneous lifetime of the upper level of the transition at $\lambda = 632 \text{ nm}$ is $\tau = 10^{-7} \text{ s}$, which gives a natural linewidth of $\delta\nu_n = 1.5 \text{ MHz}$. The vapor pressure at $T = 300 \text{ K}$ is $p(\text{I}) = 0.05 \text{ mbar}$. The pressure broadening is then about 2 MHz . Saturation broadening at a saturation parameter $S = 3$ is $\delta\nu_s = 2\delta\nu_n = 3.0 \text{ MHz}$. Transit time broadening for a laser beam diameter $2w = 1 \text{ mm}$ is $\delta\nu_{\text{tr}} = 0.4v/w \approx 120 \text{ kHz}$ for an average velocity of $v = 300 \text{ m/s}$. The total width of the Lamb dips is then $\delta\nu_{\text{LD}} = \sqrt{2^2 + 3^2 + 0.1^2} \approx 3.6 \text{ MHz}$.

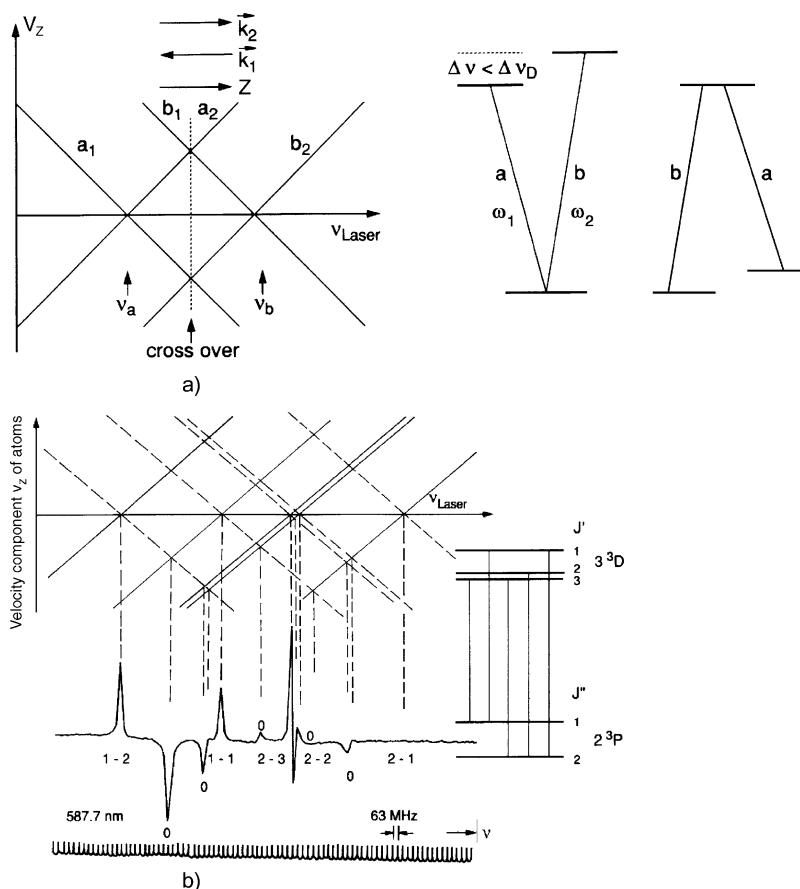


Fig. 2.14 (a) Generation of cross-over saturation signals; (b) illustration of cross-overs in the helium transition $3^3D \leftarrow 2^3P$. The cross-over signals are marked by 0 above or below the lines [215]

2.3.2 Cross-Over Signals

If two molecular transitions with a common lower or upper level overlap within their Doppler width, extra resonances, called *cross-over* signals, occur in the Lamb-dip spectrum. Their generation is explained in Fig. 2.14a.

Assume that for the center frequencies ω_1 and ω_2 of the two transitions $|\omega_1 - \omega_2| < \Delta\omega_D$ holds. At the laser frequency $\omega = (\omega_1 + \omega_2)/2$, the incident wave is shifted against ω_1 by $\Delta\omega = \omega - \omega_1 = (\omega_2 - \omega_1)/2$. If it saturates the velocity class $(v_z \pm dv_z) = (\omega_2 - \omega_1)/2k \pm \gamma k$ on the transition 1 with center frequency ω_1 , it is in resonance with molecules in this subgroup. Since the reflected wave experiences the opposite Doppler shift, when it saturates the same velocity class it is in resonance with molecules in the same subgroup in transition 2 with the center

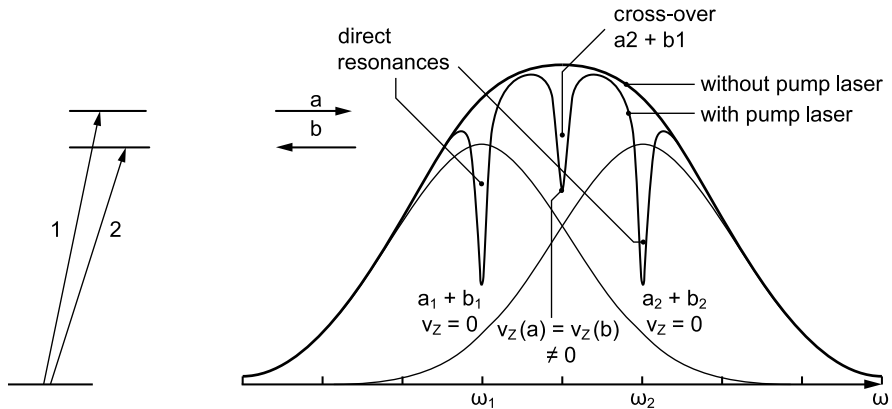


Fig. 2.15 Explanation of cross-over signals

frequency ω_2 . One therefore observes, besides the saturation signals at ω_1 and ω_2 (where the velocity class $v_z = 0$ is saturated), an additional saturation signal (cross-over) at $\omega = (\omega_1 + \omega_2)/2$ because one of the two waves causes a decrease $-\Delta N_1$ of the population density N_1 in the common lower level, which is probed by the second wave on another transition. In case of a common upper level, both waves contribute at $\omega = (\omega_1 + \omega_2)/2$ to the increase ΔN_2 of the population N_2 ; one wave on transition a, the other on b. The sign of the cross-over signals is negative for a common lower level and positive for a common upper level. Their frequency position $\omega_c = (\omega_1 + \omega_2)/2$ is just at the center between the two transitions 1 and 2 (Fig. 2.14b).

In Fig. 2.15 the three Lamb dips (two direct resonances and 1 cross-over signal) are illustrated for the case of two transitions with a common lower level. Although these cross-over signals increase the number of observed Lamb dips and may therefore increase the complexity of the spectrum, they have the great advantage that they allow one to assign pairs of transitions with a common level. This may also facilitate the assignment of the whole spectrum; see, for example, Fig. 2.14b and [205, 214–216].

2.3.3 Intracavity Saturation Spectroscopy

When the absorbing sample is placed inside the resonator of a tunable laser, the Lamb dip in the absorption coefficient $\alpha(\omega)$ causes a corresponding peak of the laser output power $P(\omega)$ (Fig. 2.16).

The power $P(\omega)$ depends on the spectral gain profile $G(\omega)$ and on the absorption profile $\alpha(\omega)$ of the intracavity sample, which is generally Doppler broadened. The Lamb peaks therefore sit on a broad background (Fig. 2.16a). With the center frequency ω_1 of the gain profile and an absorption Lamb dip at ω_0 we obtain,

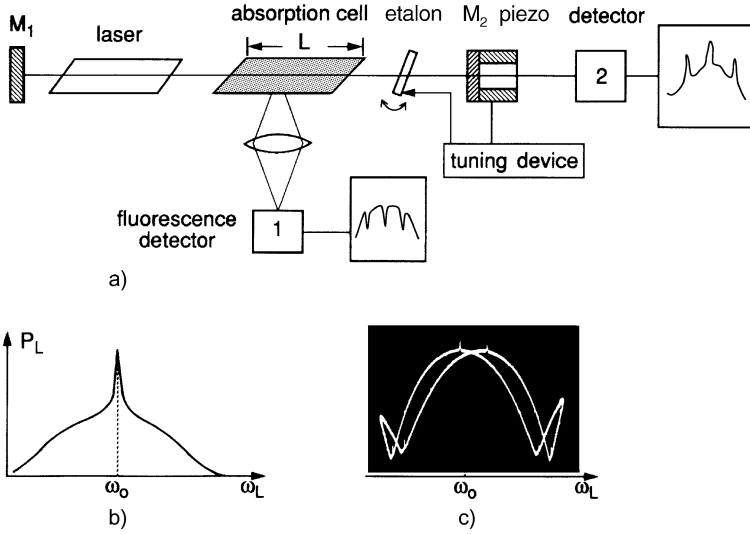


Fig. 2.16 Saturation spectroscopy inside the cavity of a laser: (a) experimental arrangement; (b) output power $P(\omega)$; (c) experimental detection of the Lamb peak in the output power of a HeNe laser tunable around $\lambda = 3.39 \mu\text{m}$, caused by the Lamb dip of a CH_4 transition in a methane cell inside the laser cavity [221]

according to Vol. 1, (5.58) and (2.35a, 2.35b)

$$P_L(\omega) \propto \left\{ G(\omega - \omega_1) - \alpha^0(\omega) \left[1 - \frac{S_0}{2} \left(1 + \frac{(\gamma_s/2)^2}{(\omega - \omega_0)^2 + (\gamma_s/2)^2} \right) \right] \right\}. \quad (2.40)$$

In a small interval around ω_0 we may approximate the gain profile $G(\omega - \omega_1)$ and the unsaturated absorption profile $\alpha^0(\omega)$ by a quadratic function of ω , yielding for (2.40) the approximation

$$P_L(\omega) = A\omega^2 + B\omega + C + \frac{D}{(\omega - \omega_0)^2 + (\gamma_s/2)^2}, \quad (2.41)$$

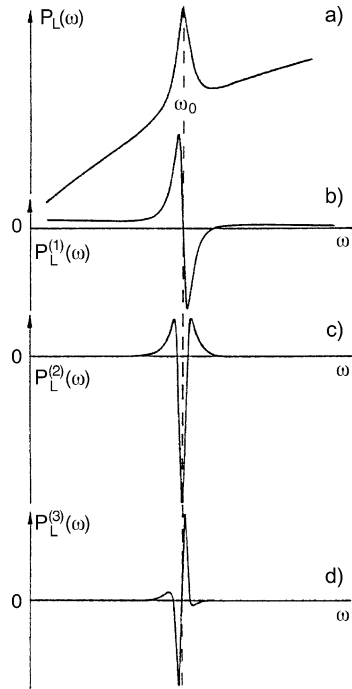
where the constants A , B , C , and D depend on ω_0 , ω_1 , γ , and S_0 . The derivatives

$$P_L^{(n)}(\omega) = \frac{d^n P_L(\omega)}{d\omega^n} \quad (n = 1, 2, 3, \dots),$$

of the laser output power with respect to ω are

$$\begin{aligned} P_L^{(1)}(\omega) &= 2A\omega + B - \frac{2D(\omega - \omega_0)}{[(\omega - \omega_0)^2 + (\gamma_s/2)^2]^2}, \\ P_L^{(2)}(\omega) &= 2A + \frac{6D(\omega - \omega_0)^2 - 2D(\gamma_s/2)^2}{[(\omega - \omega_0)^2 + (\gamma_s/2)^2]^3}, \end{aligned} \quad (2.42)$$

Fig. 2.17 Lamb peak at the slope of the Doppler-broadened gain profile and the first three derivatives, illustrating the suppression of the Doppler background



$$P_L^{(3)}(\omega) = \frac{24D(\omega - \omega_0)[(\omega - \omega_0)^2 - (\gamma_s/2)^2]}{[(\omega - \omega_0)^2 + (\gamma_s/2)^2]^4}.$$

These derivatives are exhibited in Fig. 2.17, which illustrates that the broad background disappears for the higher derivatives. If the absorptive medium is the same as the gain medium, the Lamb peak appears at the center of the gain profile (Fig. 2.16b, c).

Example 2.6 The zero crossings of $P_L^{(3)}(\omega_m)$ are at $\omega = \omega_0$ and $\omega = \omega_0 \pm \gamma_s/2$. The maxima and minima can be calculated from the condition $P_L^{(4)}(\omega_m) = 0$. The two largest central extremes are at $\omega_{m,1,2} = \omega_0 \pm 0.16\gamma_s$. The frequency difference between these extremes is then $\delta\omega = 0.32\gamma_s$. It is three times smaller than the width between the maximum and minimum of $P_L^{(1)}$. The small maximum and minimum are at $\omega = \omega_0 \pm 0.68\gamma_s$.

If the laser frequency ω is modulated at the frequency Ω , the laser output

$$P_L(\omega) = P_L(\omega_0 + a \sin \Omega t),$$

Fig. 2.18 Schematic arrangement for third-derivative intracavity saturation spectroscopy

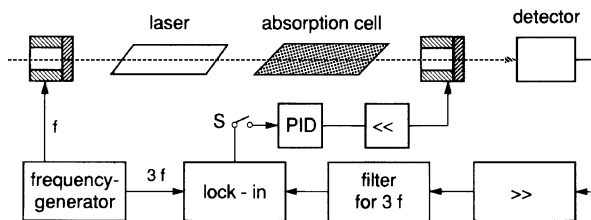
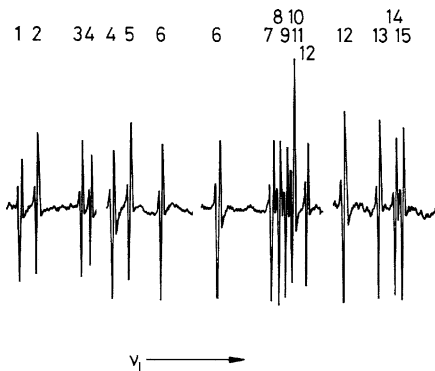


Fig. 2.19 The third-derivative intracavity absorption spectrum of I_2 around $\lambda = 514$ nm, showing the same hfs components as Fig. 2.13 [216]



can be expanded into a Taylor series around ω_0 . The derivation in Sect. 1.2.2 shows that the output $P_L(\omega, 3\Omega)$ measured with a lock-in device at the frequency 3Ω is proportional to the third derivative, see (1.13).

The experimental performance is depicted in Fig. 2.18. The modulation frequency $\Omega = 2\pi f$ is tripled by forming rectangular pulses, where the third harmonic is filtered and fed into the reference input of a lock-in amplifier that is tuned to 3Ω . Figure 2.19 illustrates this technique by the third-derivative spectrum of the same hfs components of I_2 as obtained with the intermodulated fluorescence technique in Fig. 2.13.

2.3.4 Lamb-Dip Frequency Stabilization of Lasers

The steep zero crossing of the third derivative of narrow Lamb dips gives a good reference for accurate stabilization of the laser frequency onto an atomic or molecular transition. Either the Lamb dip in the gain profile of the laser transition or Lamb dips of absorption lines of an intracavity sample can be used.

In the infrared spectral range, Lamb dips of a vibration–rotation transition of CH_4 at $\lambda = 3.39$ μm or of CO_2 around 10 μm are commonly used for frequency stabilization of the HeNe laser at 3.39 μm or the CO_2 laser. In the visible range various hyperfine components of rotational lines within the $^1\Sigma_g \rightarrow ^3\Pi_{0u}$ system of the I_2 molecule are mainly chosen. The experimental setup is the same as that shown in Fig. 2.18. The laser is tuned to the wanted hfs component and then the

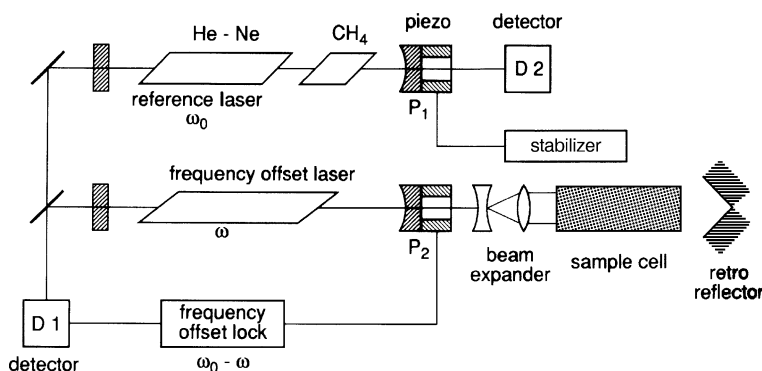


Fig. 2.20 Schematic diagram of a frequency-offset locked laser spectrometer

feedback switch S is closed in order to lock the laser onto the zero crossing of this component [217].

Using a double servo loop for fast stabilization of the laser frequency onto the transmission peak of a Fabry–Perot Interferometer (FPI) and a slow loop to stabilize the FPI onto the first derivative of a forbidden narrow calcium transition, Barger et al. constructed an ultrastable cw dye laser with a short-term linewidth of approximately 800 Hz and a long-term drift of less than 2 kHz/h [218]. Stabilities of better than 1 Hz have also been realized [219, 220].

This extremely high stability can be transferred to tunable lasers by a special *frequency-offset locking* technique [221]. Its basic principle is illustrated in Fig. 2.20. A reference laser is frequency stabilized onto the Lamb dip of a molecular transition at ω_0 . The output from a second, more powerful laser at the frequency ω is mixed in detector D1 with the output from the reference laser at the frequency ω_0 . An electronic device compares the difference frequency $\omega_0 - \omega$ with the frequency ω' of a stable but tunable RF oscillator, and controls the piezo P2 such that $\omega_0 - \omega = \omega'$ at all times. The frequency ω of the powerful laser is therefore always locked to the *offset frequency* $\omega = \omega_0 - \omega'$, which can be controlled by tuning the RF frequency ω' .

For Lamb-dip spectroscopy with ultrahigh resolution, the output beam of the powerful laser is expanded before it is sent through the sample cell in order to minimize transit-time broadening (Vol. 1, Sect. 3.4). A retroreflector provides the counterpropagating probe wave for Lamb-dip spectroscopy. The real experimental setup is somewhat more complicated. A third laser is used to eliminate the troublesome region near the zero-offset frequency. Furthermore, optical decoupling elements have to be inserted to avoid optical feedback between the three lasers. A detailed description of the whole system can be found in [222].

An outstanding example of the amount of information on interactions in a large molecule that can be extracted from a high-resolution spectrum is represented by the work of Bordé et al. on saturation spectroscopy of SF₆ [223]. Many details of the various interactions, such as spin-rotation coupling, Coriolis coupling, and hyperfine structure, which are completely masked at lower resolution, can be unravelled when

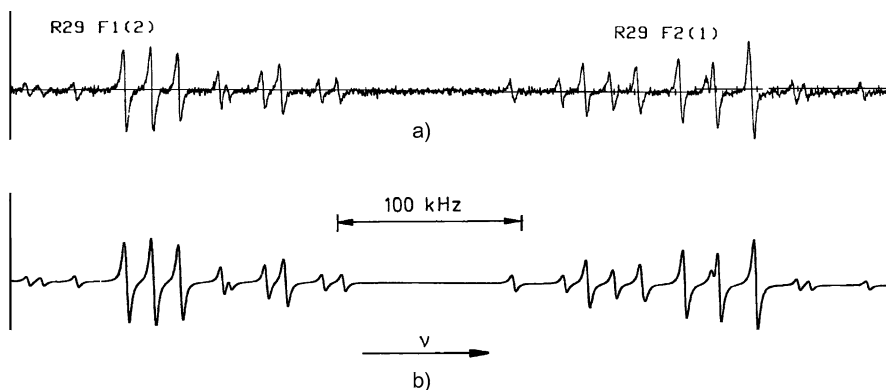


Fig. 2.21 Hyperfine and super-hyperfine structures of a rotational–vibrational transition in SF_6 , showing the molecular transitions and cross-over signals: (a) experimental spectrum; (b) calculated spectrum [223]

sufficiently high resolution is achieved. For illustration Fig. 2.21 depicts a section of the saturation spectrum of SF_6 taken by this group.

Meanwhile, many complex molecular spectra have been resolved by saturation spectroscopy. One example are the ultranarrow overtone transitions of the acetylene isotopomer $^{13}\text{C}_2\text{H}_2$ [224].

2.4 Polarization Spectroscopy

While saturation spectroscopy monitors the decrease of *absorption* of a probe beam caused by a pump wave that has selectively depleted the absorbing level, the signals in polarization spectroscopy come mainly from the change of the *polarization state* of the probe wave induced by a *polarized* pump wave. Because of optical pumping, the pump wave causes not only a change in the absorption coefficient α , but also a change in the refraction index n .

This very sensitive Doppler-free spectroscopic technique has many advantages over conventional saturation spectroscopy and will certainly gain increasing attention [225, 226]. We therefore discuss the basic principle and some of its experimental modifications in more detail.

2.4.1 Basic Principle

The basic idea of polarization spectroscopy can be understood in a simple way (Fig. 2.22). The output from a monochromatic tunable laser is split into a weak probe beam with the intensity I_1 and a stronger pump beam with the intensity I_2 . The probe beam passes through a linear polarizer P_1 , the sample cell, and a second

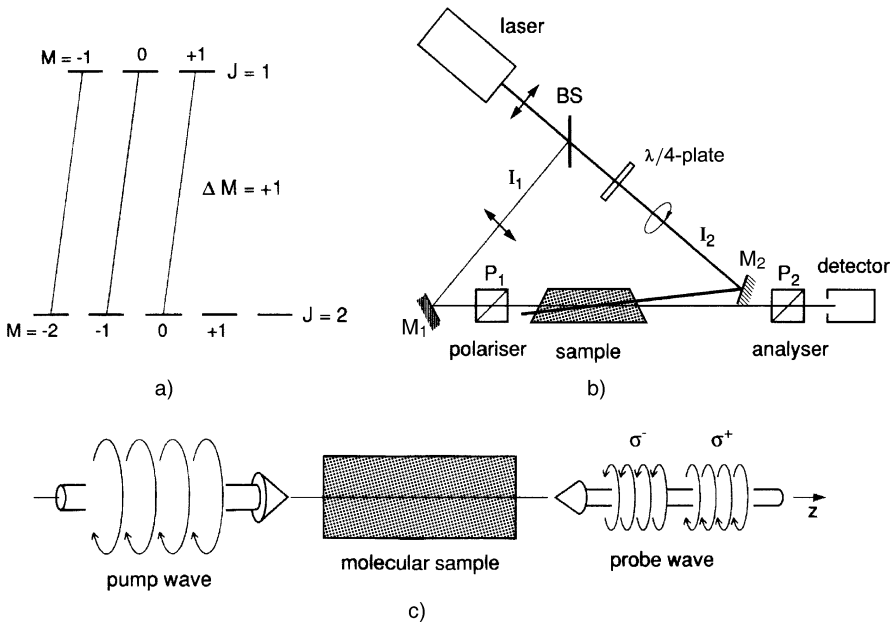


Fig. 2.22 Polarization spectroscopy: (a) level scheme for a P transition $J = 2 \rightarrow J = 1$; (b) experimental setup; (c) linearly polarized probe wave as superposition of σ^+ (angular momentum $+5$ in z -direction) and σ^- components

linear polarizer P_2 , which is crossed with P_1 . Without the pump laser, the sample is isotropic and therefore does not change the polarisation of the probe beam. The detector D behind P_2 receives only a very small signal caused by the residual transmission of the crossed polarizer, which might be as small as $10^{-8} I_1$.

After having passed through a $\lambda/4$ -plate, which produces a circular polarization, the pump beam travels in the opposite direction through the sample cell. When the laser frequency ω is tuned to a molecular transition $(J'', M'') \rightarrow (J', M')$, molecules in the lower level (J'', M'') can absorb the pump wave. The quantum number M that describes the projection of J onto the direction of light propagation follows the selection rule $\Delta M = +1$ for the transitions $M'' \rightarrow M'$ induced by σ^+ circularly polarized light ($M'' \rightarrow M' = M'' + 1$). The degenerate M'' sublevels of the rotational level J'' become partially or completely depleted because of saturation. The degree of depletion depends on the pump intensity I_2 , the absorption cross section $\sigma(J'', M'' \rightarrow J', M')$, and on possible relaxation processes that may repopulate the level (J'', M'') . The cross section σ depends on J'', M'', J' , and M' . From Fig. 2.22a it can be seen that in the case of P-transitions ($\Delta J = -1$), not all of the M'' sublevels of the lower state are pumped. For example, from levels with $M'' = +J''$ no P-transitions with $\Delta M = +1$ are possible, while for R-transitions the levels $M' = -J'$ in the upper state are not populated. *This implies that the pumping process produces an unequal saturation and with it a nonuniform population of*

the M sublevels, which is equivalent to an anisotropic distribution for the orientations of the angular momentum vector J .

Such an anisotropic sample becomes birefringent for the incident linearly polarized probe beam. Its plane of polarization is slightly rotated after having passed the anisotropic sample. This effect is quite analogous to the Faraday effect, where the nonisotropic orientation of J is caused by an external magnetic field. For polarization spectroscopy no magnetic field is needed. Contrary to the Faraday effect where all molecules are oriented, here only those molecules that interact with the monochromatic pump wave show this nonisotropic orientation. As has already been discussed in Sect. 2.2, this is the subgroup of molecules with the velocity components

$$v_z \pm \Delta v_z = (\omega_0 - \omega)/k \pm \gamma/k,$$

where Δv_z is determined by the homogeneous linewidth $\delta\omega = \gamma$.

For $\omega \neq \omega_0$ the probe wave that passes in the opposite direction through the sample interacts with a *different group* of molecules in the velocity interval $v_z \pm \Delta v_z = -(\omega_0 - \omega \pm \delta\omega)/k$, and will therefore not be influenced by the pump wave. If, however, the laser frequency ω coincides with the center frequency ω_0 of the molecular transition within its homogeneous linewidth $\delta\omega = \gamma$ (i.e., $\omega = \omega_0 \pm \delta\omega \rightarrow v_z = 0 \pm \Delta v_z$), both waves can be absorbed by the same molecules and the probe wave experiences a birefringence from the nonisotropic M distribution of the molecules in the absorbing lower rotational level J'' or in the upper level J' .

Only in this case will the plane of polarization of the probe wave be slightly rotated by $\Delta\theta$, and the detector D will receive a Doppler-free signal every time the laser frequency ω is tuned across the center of a molecular absorption line.

2.4.2 Line Profiles of Polarization Signals

Let us now discuss the generation of this signal in a more quantitative way. The linearly polarized probe wave

$$\mathbf{E} = E_0 e^{i(\omega t - kz)}, \quad E_0 = \{E_0, 0, 0\},$$

can always be composed of a σ^+ and a σ^- circularly polarized component $\mathbf{E} = \mathbf{E}^+ + \mathbf{E}^-$ (Fig. 2.22c) where

$$E^+ = E_0^+ e^{i(\omega t - k^+ z)}, \quad E_0^+ = \frac{1}{2} E_0 (\hat{x} + i\hat{y}), \quad (2.43a)$$

$$E^- = E_0^- e^{i(\omega t - k^- z)}, \quad E_0^- = \frac{1}{2} E_0 (\hat{x} - i\hat{y}), \quad (2.43b)$$

where \hat{x} and \hat{y} are unit vectors in the x - and y -direction, respectively. While passing through the birefringent sample the two components experience different absorption

coefficients α^+ and α^- and different refractive indices n^+ and n^- from the non-isotropic saturation caused by the σ^+ -polarized pump wave. The refractive indices n^+ , n^- are related to the wave numbers $k = 2\pi/\lambda$ by $n^+ = ck^+/\omega$, $n^- = ck^-/\omega$. After a path length L through the pumped region of the sample, the two components are

$$\begin{aligned} E^+ &= E_0^+ e^{i[\omega t - k^+ L + i(\alpha^+/2)L]}, \\ E^- &= E_0^- e^{i[\omega t - k^- L + i(\alpha^-/2)L]}. \end{aligned} \quad (2.44)$$

Because of the differences $\Delta n = n^+ - n^-$ and $\Delta\alpha = \alpha^+ - \alpha^-$ caused by the non-isotropic saturation, a phase difference

$$\Delta\phi = (k^+ - k^-)L = (\omega L/c)\Delta n,$$

has developed between the two components, and also a small amplitude difference

$$\Delta E = \frac{E_0}{2} [e^{-(\alpha^+/2)L} - e^{-(\alpha^-/2)L}].$$

The windows of the absorption cell with thickness d also show a small absorption and a pressure-induced birefringence from the atmospheric pressure on one side and vacuum on the other side. Their index of refraction n_w and their absorption coefficient α_w can be expressed by the complex quantity

$$n_w^{*\pm} = b_r^\pm + i b_i^\pm, \quad \text{with } n_w = b_r, \quad \text{and} \quad \alpha_w = 2k \cdot b_i = 2(\omega/c)b_i.$$

Behind the exit window the superposition of the σ^+ and σ^- components of the linearly polarized probe wave traveling into the z -direction yields the elliptically polarized wave

$$\begin{aligned} E(z=L) &= E^+ + E^- \\ &= \frac{1}{2} E_0 e^{i\omega t} e^{-i[\omega(nL+b_r)/c - i\alpha L/2 - i a_w/2]} \\ &\quad \times [(\hat{x} + i\hat{y})e^{-i\delta} + (\hat{x} - i\hat{y})e^{+i\delta}], \end{aligned} \quad (2.45)$$

where $a_w = 2d\alpha_w = (4d \cdot \omega/c)b_i$ is the absorption in the two windows of the sample cell, and

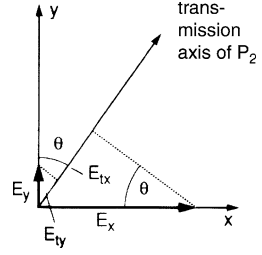
$$n = \frac{1}{2}(n^+ + n^-); \quad \alpha = \frac{1}{2}(\alpha^+ + \alpha^-); \quad b = \frac{1}{2}(b^+ + b^-)$$

are the average quantities. The phase factor

$$\delta = \omega(L\Delta n + \Delta b_r)/2c - i(L\Delta\alpha/4 + \Delta a_w/2),$$

depends on the differences

Fig. 2.23 Transmission of the elliptically polarized probe wave through the analyzer, uncrossed by the angle θ



$$\Delta n = n^+ - n^-, \quad \Delta \alpha = \alpha^+ - \alpha^-, \quad \Delta b_r = b_r^+ - b_r^-, \quad \text{and} \\ \Delta b_i = b_i^+ - b_i^-.$$

If the transmission axis of the analyzer P_2 is tilted by the small angle $\theta \ll 1$ against the y-axis (Fig. 2.23) the transmitted amplitude becomes

$$E_t = E_x \sin \theta + E_y \cos \theta.$$

For most practical cases, the differences $\Delta \alpha$ and Δn caused by the pump wave are very small. Also, the birefringence of the cell windows can be minimized (for example, by compensating the air pressure by a mechanical pressure onto the edges of the windows). With

$$L \Delta \alpha \ll 1, \quad L \Delta k \ll 1, \quad \text{and} \quad \Delta b \ll 1,$$

we can expand $\exp(i\delta)$ in (2.45). We then obtain for small angles $\theta \ll 1$ ($\cos \theta \approx 1$, $\sin \theta \approx \theta$) the transmitted amplitude

$$E_t = E_0 e^{i\omega t} \exp \left[-i \left\{ \omega(nL + b_r)/c - \frac{i}{2}(\alpha \cdot L + a_w) \right\} \right] (\theta + \delta). \quad (2.46)$$

The detector signal $S(\omega)$ is proportional to the transmitted intensity

$$S(\omega) \propto I_T(\omega) = c \epsilon_0 E_t E_t^*.$$

Even for $\theta = 0$ the crossed polarizers have a small residual transmission $I_t = \xi I_0$ ($\xi \approx 10^{-6}$ to 10^{-8}). Taking this into account, we obtain with the incident probe intensity I_0 and the abbreviation $\theta' = \theta + \omega/(2c) \cdot \Delta b_r$ and $a_w = 2d\alpha_w = 4dkb_i$, the transmitted intensity

$$\begin{aligned} I_t &= I_0 e^{-\alpha L - a_w} (\xi + |\theta + \Delta|^2), \\ &= I_0 e^{-\alpha L - a_w} \left[\xi + \theta'^2 + \left(\frac{1}{2} \Delta a_w \right)^2 + \frac{1}{4} \Delta a_w L \Delta \alpha + \frac{\omega}{c} \theta' L \Delta n \right. \\ &\quad \left. + \left(\frac{\omega}{2c} L \Delta n \right)^2 + \left(\frac{L \Delta \alpha}{4} \right)^2 \right]. \end{aligned} \quad (2.47)$$

The change of absorption $\Delta\alpha$ is caused by those molecules within the velocity interval $\Delta v_z = 0 \pm \gamma_s/k$ that simultaneously interact with the pump and probe waves. The line profile of $\Delta\alpha(\omega)$ is therefore, analogous to the situation in saturation spectroscopy (Sect. 2.2) a Lorentzian profile

$$\Delta\alpha(\omega) = \frac{\Delta\alpha_0}{1+x^2}, \quad \text{with } x = \frac{\omega_0 - \omega}{\gamma_s/2}, \quad \text{and } \alpha_0 = \alpha(\omega_0), \quad (2.48)$$

having the halfwidth γ_s , which corresponds to the homogeneous width of the molecular transition saturated by the pump wave.

The absorption coefficient $\alpha(\omega)$ and the refractive index $n(\omega)$ are related by the Kramers–Kronig dispersion relation, see (3.36b, 3.37b) in Vol. 1, Sect. 3.1.

We therefore obtain for $\Delta n(\omega)$ the dispersion profile

$$\Delta n(\omega) = \frac{c}{\omega_0} \frac{\Delta\alpha_0 x}{1+x^2}. \quad (2.49)$$

Inserting (2.48 and 2.49) into (2.47) gives for the *circularly polarized pump beam* the line profile of the detector signal

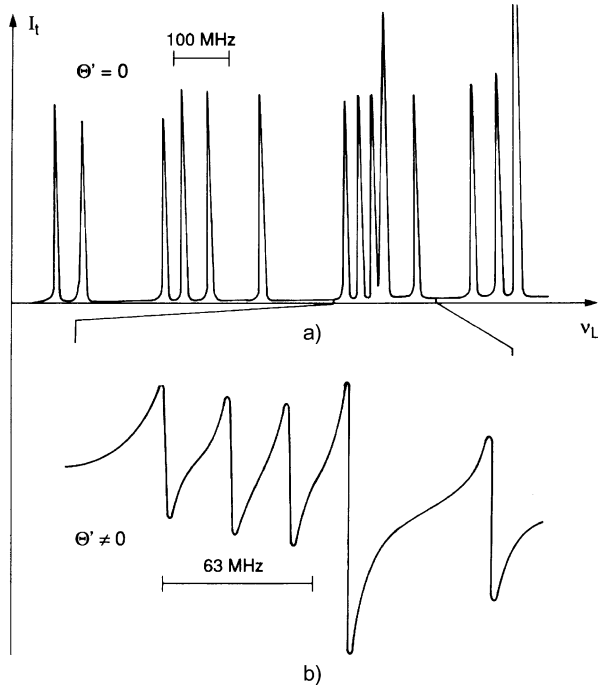
$$\begin{aligned} S^{\text{cp}} = I_t(\omega) = I_0 e^{-\alpha L - a_w} & \left\{ \xi + \theta'^2 + \frac{1}{4} \Delta a_w^2 + \frac{1}{2} \theta' \Delta\alpha_0 L \frac{x}{1+x^2} \right. \\ & \left. + \left[\frac{1}{4} \Delta\alpha_0 \Delta a_w L + \left(\frac{\Delta\alpha_0 L}{4} \right)^2 \right] \frac{1}{1+x^2} + \frac{3}{4} \left(\frac{\Delta\alpha_0 x}{(1+x^2)} \right)^2 \right\}. \end{aligned} \quad (2.50)$$

The signal contains a constant background term $\xi + \theta'^2 + \Delta a_w^2/4$ that is independent of the frequency ω . The quantity $\xi = I_T/I_0$ ($\theta = 0$, $\Delta a_w = \Delta b_r = 0$, $\Delta\alpha_0 = 0$) gives the residual transmission of the completely crossed analyzer P_2 . With normal Glan–Thomson polarizers $\xi < 10^{-6}$ can be realized, with selected samples even $\xi < 10^{-8}$ can be obtained. The third term is due to the absorption part of the window birefringence. All these three terms are approximately independent of the frequency ω .

The next three terms contribute to the line profile of the polarization signal. The first frequency-dependent term in (2.50) gives the additional transmitted intensity when the angle $\theta' = \theta + (\omega/2c)\Delta b_r$ is not zero. It has a dispersion-type profile. For $\theta' = 0$ the dispersion term vanishes. The two Lorentzian terms depend on the product of Δa_w and $\Delta\alpha_0 \cdot L$ and on $(\Delta\alpha_0 L)^2$. By squeezing the windows their dichroism (that is, Δa_w) can be increased and the amplitude of the first Lorentzian term can be enlarged. Of course, the background term Δa_w^2 also increases and one has to find the optimum signal-to-noise ratio. Since in most cases $\Delta\alpha_0 L \ll 1$, the last term in (2.50), which is proportional to $\Delta\alpha_0^2 L^2$, is generally negligible. Nearly pure dispersion signals can be obtained if Δa_w is minimized and θ' is increased until the optimum signal-to-noise ratio is achieved. Therefore by controlling the birefringence of the window either dispersion-shaped or Lorentzian line profiles can be obtained for the signals.

The sensitivity of polarization spectroscopy compared with saturation spectroscopy is illustrated by Fig. 2.24a, which shows the same hfs transitions of I_2

Fig. 2.24 Polarization spectrum of the same hyperfine components of I_2 as shown in Fig. 2.13 with circularly polarized pump: (a) with $\theta' = 0$; (b) enlarged section with $\theta' \neq 0$



as in Fig. 2.13 taken under comparable experimental conditions. A section of the same spectrum is depicted in Fig. 2.24b with $\theta' \neq 0$, optimized for dispersion line-profiles.

If the pump wave is *linearly polarized* with the electric field vector 45° against the x -axis, one obtains in an analogous derivation for the polarization signal instead of (2.50) the expression

$$S^{LP}(\omega) = I_0 e^{-\alpha L - a_w} \left\{ \xi + \frac{1}{4} \theta^2 \Delta a_w^2 + \left(\frac{\omega}{2c} \Delta b_r \right)^2 + \frac{\Delta b_r}{4} \frac{\omega}{c} \Delta \alpha_0 L \frac{x}{1+x^2} + \left[-\frac{1}{4} \theta \Delta a_w \Delta \alpha_0 L + \left(\frac{\Delta \alpha_0 L}{4} \right)^2 \right] \frac{1}{1+x^2} \right\}, \quad (2.51)$$

where $\Delta \alpha = \alpha_{\parallel} - \alpha_{\perp}$ and $\Delta b = b_{\parallel} - b_{\perp}$ are now defined by the difference of the components parallel or perpendicular to the \mathbf{E} vector of the pump wave. Dispersion and Lorentzian terms as well as Δa_w and Δb_r are interchanged compared with (2.50). If two different lasers are used as pump and probe, all probe transitions which share a common lower or upper level with the pump transition are accessible to polarisation spectroscopy. Therefore P- and R-transitions can be probed, even if the pump is stabilized on a Q-transition. In Fig. 2.25 the different possibilities are illustrated (see also Chap. 5).

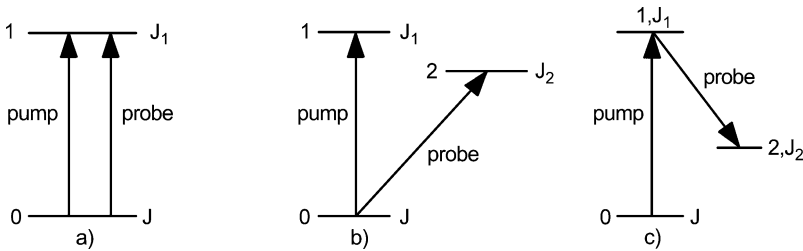


Fig. 2.25 Level scheme for possible pump-probe experiments. (a) Two-level scheme; (b) V-type scheme with three-level scheme; (c) Δ -type scheme

2.4.3 Magnitude of Polarization Signals

In order to understand the different magnitudes and line profiles, we have to investigate the magnitudes of the differences $\Delta\alpha_0 = \alpha^+ - \alpha^-$ for a circularly polarized pump wave and $\Delta\alpha_0 = \alpha_{\parallel} - \alpha_{\perp}$ for a linearly polarized pump wave, and their relation to the absorption cross section of the molecular transitions.

When a linearly polarized weak probe wave propagating through an ensemble of molecules is tuned to a molecular transition $|J, M\rangle \rightarrow |J_1, M \pm 1\rangle$, the difference $\Delta\alpha = \alpha^+ - \alpha^-$ of the absorption coefficients of its left- and right-hand circularly polarized components is

$$\Delta\alpha(M) = N_M(\sigma_{JJ_1M}^+ - \sigma_{JJ_1M}^-), \quad (2.52)$$

where $N_M = N_J/(2J + 1)$ represents the population density of one of the $(2J + 1)$ degenerate sublevels $|J, M\rangle$ of a rotational level $|J\rangle$ in the lower state, and $\sigma_{JJ_1M}^{\pm}$ the absorption cross section for transitions starting from the level $|J, M\rangle$ and ending on $|J_1, M \pm 1\rangle$.

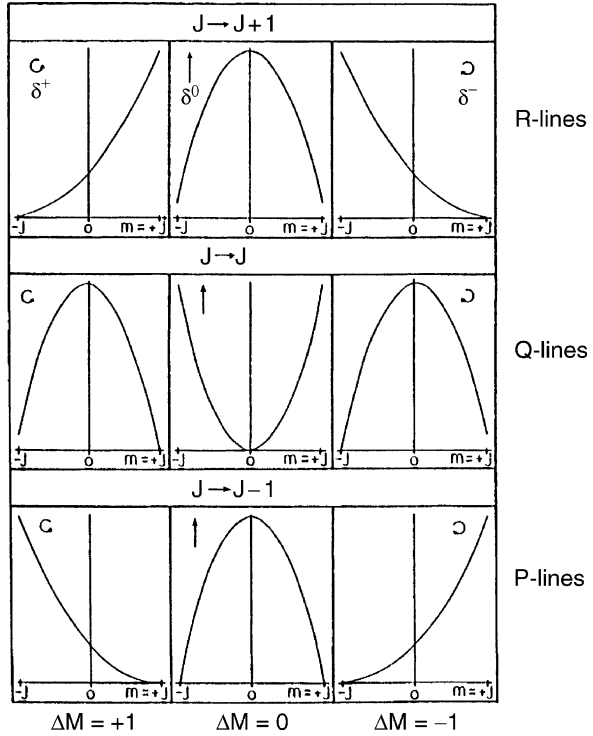
The absorption cross section

$$\sigma_{JJ_1M} = \sigma_{JJ_1} C(J, J_1, M, M_1) \quad (2.53)$$

can be separated into a product of two factors: the first factor is independent of the molecular orientation, but depends solely on the internal transition probability of the molecular transitions, which differs for P, Q, and R-lines [228, 229]. The second factor in (2.53) is the Clebsch–Gordan coefficient, which depends on the rotational quantum numbers J, J_1 of the lower and upper levels, and on the orientation of the molecule with respect to the quantization axis. In the case of a σ^+ pump wave, this is the propagation direction k_p ; in the case of a π pump wave, it is the direction of the electric vector \mathbf{E} , see Fig. 2.26.

The total change $\Delta\alpha(J \rightarrow J_1) = \alpha^+(J \rightarrow J_1) - \alpha^-(J \rightarrow J_1)$ on a rotational transition $J \rightarrow J_1$ is due to the saturation of all allowed transitions ($M_J \rightarrow M_{J_1}$ with $\Delta M = \pm 1$ for a circular pump polarization or $\Delta M = 0$ for a linearly polarized pump) between the $(2J + 1)$ degenerate sublevels M in the lower level J and the

Fig. 2.26 Dependence of σ_{JJ_1M} on the orientational quantum number M for transitions with $\Delta M = 0, \pm 1$



$(2J_1 + 1)$ sublevels in the upper level J_1 .

$$\Delta\alpha(J, J_1) = \sum_M N_M (\sigma_{JJ_1M}^+ - \sigma_{JJ_1M}^-). \quad (2.54)$$

Because of the saturation by the pump beam, the population N_M decreases from its unsaturated value N_M^0 to

$$N_M^S = \frac{N_M^0}{1 + S},$$

where the saturation parameter

$$S = \frac{B_{12}Q_2}{R^*} = \frac{8\sigma_{JJ_1M}}{\gamma_s R^*} \frac{I_2}{\hbar\omega}, \quad (2.55)$$

depends on the absorption cross section for the pump transition, the saturated homogeneous linewidth γ_s , the mean relaxation rate R^* , which refills the saturated level population (for example, by collisions) and the number of pump photons $I_2/\hbar\omega$ per cm^2 and second [227].

From (2.52–2.54) we finally obtain for the quantity $\Delta\alpha_0$ in (2.50, 2.51)

$$\Delta\alpha_0 = \alpha_0 S_0 \Delta C_{JJ_1}^*, \quad (2.56)$$

Table 2.1 Values of $\frac{2}{3}\Delta C_{J_1 J_2}^*$ for linear pump polarization (a) and circular pump polarization (b). For the two-level system $J_1 = J_2$ and $r = (\gamma_J - \gamma_{J_2})/(\gamma_J + \gamma_{J_2})$. For the three-level system J is the rotational quantum number of the common level and $r = -1$

	$J_2 = J + 1$	$J_2 = J$	$J_2 = J - 1$
(a) Linear pump polarization			
$J_1 = J + 1$	$\frac{2J^2 + J(4+5r) + 5+5r}{5(J+1)(2J+3)}$	$-\frac{(2J-1)}{5(J+1)}$	$\frac{1}{5}$
$J_1 = 1$	$-\frac{(2J-1)}{5(J+1)}$	$\frac{(2J-3)(2J-1)}{5J(J+1)}$	$-\frac{2J+3}{5J}$
$J_1 = J - 1$	$\frac{1}{5}$	$-2J + \frac{3}{5J}$	$\frac{2J^2 - 5rJ + 3}{5J(2J-1)}$
(b) Circular pump polarization			
$J_1 = J + 1$	$\frac{2J^2 + J(4+r) + r + 1}{(2J+3)(J+1)}$	$\frac{-1}{J+1}$	-1
$J_1 = 1$	$\frac{-1}{J+1}$	$\frac{1}{J(J+1)}$	$\frac{1}{J}$
$J_1 = J - 1$	-1	$\frac{1}{J}$	$\frac{2J^2 - rJ - 1}{J(2J-1)}$

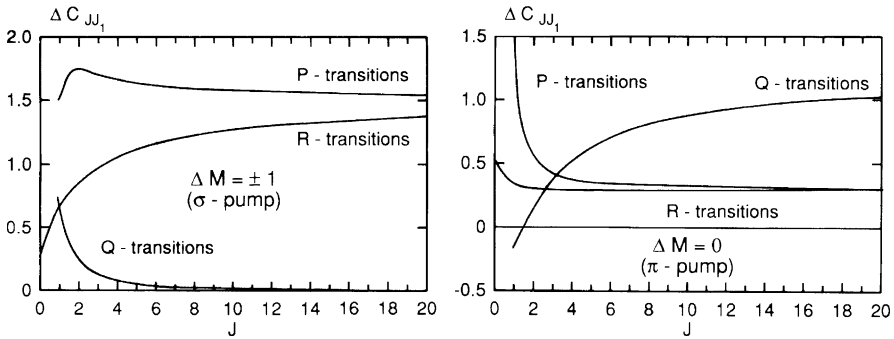
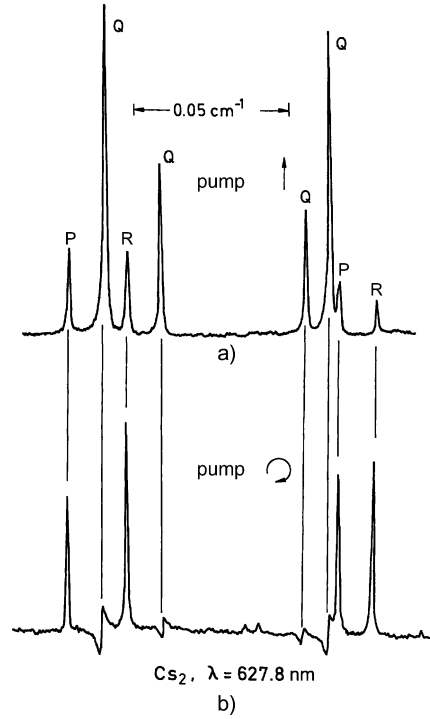


Fig. 2.27 Relative magnitude of polarization signals expressed by the factor $\Delta C_{J J_1}^*$ as a function of rotational quantum number J for circular and linear pump polarization

where $\alpha_0 = N_J \sigma_{J J_1}$ is the unsaturated absorption coefficient of the probe wave at the line center, and $\Delta C_{J J_1}^*$ is a numerical factor that is proportional to the sum $\sum \Delta \sigma_{J J_1 M} C(J J_1 M M_1)$ with $\Delta \sigma = \sigma^+ - \sigma^-$. The numerical values of $\Delta C_{J J_1}^*$ are compiled in Table 2.1 for P, Q, and R-transitions. Their dependence on the rotational quantum number J is illustrated by Fig. 2.27. As can be seen, for a linearly polarized pump Q-transitions have a larger cross section, while for circular pump polarization P and R-lines are favoured. This is advantageous for the assignment of molecular spectra. For illustration, in Fig. 2.28 two identical sections of the Cs_2 polarization spectrum around $\lambda = 627.8$ nm are shown, pumped with a linearly or circularly polarized pump beam, respectively. As shown below, the magnitude of the polarization signals for linearly polarized pump is large for transitions with $\Delta J = 0$, whereas for a circularly polarized pump they are maximum for $\Delta J = \pm 1$. While the Q-lines are

Fig. 2.28 Two identical sections of the Cs_2 polarization spectrum recorded with linear (*upper spectrum*) and circular pump polarization (*lower spectrum*)



prominent in the upper spectrum, they appear in the lower spectrum only as small dispersion-type signals.

2.4.4 Sensitivity of Polarization Spectroscopy

In the following we briefly discuss the sensitivity and the signal-to-noise ratio achievable with polarization spectroscopy. The amplitude of the dispersion signal in (2.50) for $\theta' \neq 0$ is approximately the difference $\Delta I_T = I_T(x = +1) - I_T(x = -1)$ between the maximum and the minimum of the dispersion curve. From (2.50) we obtain (Fig. 2.29)

$$\Delta S_{\max} = I_0 e^{-(\alpha L + a_w)} \cdot \theta' \Delta \alpha_0 L, \quad (2.57a)$$

while for the Lorentzian profiles ($I_T(x = 0) - I_T(x = \infty)$, $\theta' = 0$) we derive from (2.50)

$$\Delta S_{\max} = I_0 e^{-(\alpha L + a_w)} \cdot \frac{\Delta \alpha_0 L}{4} \left(\Delta a_w + \frac{1}{4} \Delta \alpha_0 L \right). \quad (2.57b)$$

Under general laboratory conditions the main contribution to the noise comes from fluctuations of the probe-laser intensity, while the principal limit set by shot noise

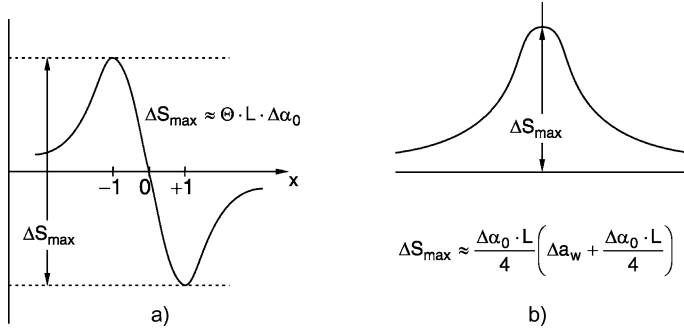


Fig. 2.29 Magnitude of signals in polarization spectroscopy: **(a)** for dispersion signals; **(b)** for Lorentzian signals

(Chap. 4) is seldom reached. The noise level is therefore essentially proportional to the transmitted intensity, which is given by the background term in (2.50).

Because the crossed polarizers greatly reduce the background level, we can expect a better signal-to-noise ratio than in saturation spectroscopy, where the full intensity of the probe beam is detected.

In the absence of window birefringence (that is, $\Delta b_r = \Delta b_i = 0$, $\theta' = \theta$) the signal-to-noise (S/N) ratio, which is, besides a constant factor a , equal to the signal-to-background ratio, becomes with (2.56) and (2.57a) for the dispersion signals

$$\frac{S}{N} = a \frac{\theta \alpha_0 L S_0}{\xi + \theta^2} \Delta C_{JJ_1}^*, \quad (2.58)$$

where a is a measure of the intensity stability of the probe laser, i.e., I_1/a is the mean noise of the incident probe wave with intensity I_1 , and S_0 is the saturation parameter at $\omega = \omega_0$.

This ratio is a function of the uncrossing angle θ of the two polarizers (Fig. 2.23) and has a maximum for $d(S/N)/d\theta = 0$, which yields $\theta^2 = \xi$ and

$$\left(\frac{S}{N} \right)_{\max} = a \frac{\alpha_0 L S_0 \Delta C_{JJ_1}^*}{2\sqrt{\xi}}. \quad (2.59)$$

In this case of ideal windows ($b_r = b_i = 0$) the quality of the two polarizers, given by the residual transmission ξ of the completely crossed polarizations ($\theta = 0$), limits the achievable S/N ratio.

For comparison, in saturation spectroscopy the S/N ratio is, according to (2.37), given by

$$\frac{S}{N} = \frac{\alpha_0 S_0 L I_0 a}{2I_0} = \frac{1}{2} a \alpha_0 L S_0. \quad (2.60)$$

Polarization spectroscopy therefore increases the S/N ratio by the factor $\Delta C_{JJ_1}^* / 2\sqrt{\xi}$ for optimized dispersion-type signals.

Example 2.7 For $\Delta C_{JJ_1}^* = 0.5$, $\xi = 10^{-6}$, the S/N ratio in polarization spectroscopy with ideal cell windows becomes 500 times better than in saturation spectroscopy.

For windows with birefringence the situation is more complex: for $b_r = 0$ we obtain for the dispersion signals the optimum uncrossing angle

$$\theta' = \sqrt{\xi + \left(\frac{1}{2}\Delta a_w\right)^2}. \quad (2.61)$$

This yields the maximum obtainable signal-to-noise ratio for dispersion signals

$$\left(\frac{S}{N}\right)_{\max}^{\text{disp}} = a \cdot \alpha_0 \cdot L S_0 \cdot \Delta C_{JJ_1}^* \frac{1}{2 \cdot \sqrt{\xi + (\frac{1}{2}\Delta a_w)}}, \quad (2.62)$$

which converts to (2.59) for $\Delta a_w = 0$.

Example 2.8 For $\xi = 10^{-6}$ and $\Delta a_w = 10^{-5}$, the S/N ratio is smaller than in Example 2.7 by a factor of 0.4. For $\xi = 10^{-8}$ one reaches an improvement in the S/N compared to saturation spectroscopy by a factor of 5000 with $\Delta a_w = 0$, but only 150 for $\Delta a_w = 10^{-5}$.

For the Lorentzian line profiles with $\theta' = 0$ in (2.50) we obtain

$$\left(\frac{S}{N}\right)_{\max} = \frac{a}{4} \frac{\Delta \alpha_0 L (\Delta a_w + \Delta \alpha_0 L / 4)}{\xi + (\Delta a_w / 2)^2}. \quad (2.63)$$

Here we have to optimize Δa_w to achieve the maximum S/N ratio. The differentiation of (2.63) with respect to Δa_w gives for $\xi \ll \Delta \alpha \cdot L$ the optimum window birefringence

$$\Delta a_w \approx \frac{4\xi}{\Delta \alpha_0 \cdot L}, \quad (2.64)$$

which yields for the maximum S/N ratio for Lorentzian signals

$$\boxed{\left(\frac{S}{N}\right)_{\max} \approx a \cdot \alpha_0 L S_0 \Delta C_{JJ_1}^* \cdot \frac{\Delta \alpha_0 L}{4\xi} \left(1 + \frac{12\xi}{(\Delta \alpha_0 L)^2} - \frac{64\xi^2}{(\Delta \alpha_0 L)^3}\right)}. \quad (2.65)$$

Example 2.9 With $a = 10^2$, $\xi = 10^{-6}$, $\Delta C_{JJ_1}^* = 0.5$, $\alpha_0 L = 10^{-2}$, and $S_0 = 0.1$, we obtain a signal-to-noise ratio of $5\alpha_0 \cdot L = 5 \times 10^{-2}$ for the saturation spectroscopy signal measured with the arrangement in Fig. 2.10, without lock-in detection but $S/N = 2.5 \times 10^3 \alpha_0 \cdot L = 25$ for the dispersion signal or the optimized Lorentzian profiles in polarization spectroscopy. In practice, these figures are somewhat lower because $\Delta a_w \neq 0$. One must also take into account that the length L of the interaction zone is smaller in the arrangement of Fig. 2.22 (because of the finite angle between the pump and probe beams) than for saturation spectroscopy with completely overlapping pump and probe beams (Fig. 4.12). For $\alpha_0 L = 10^{-3}$ and $\xi = 10^{-6}$, one still achieves $S/N \approx 2.5$ for dispersion and for Lorentzian signals. For $\xi = 10^{-8}$ and $\Delta a_w = 10^{-4}$, the improvement factor over saturation spectroscopy is 70 for dispersion signals. For Lorentzian signals, the optimum value of $\Delta \alpha_w$ is 4×10^{-6} for $\Delta \alpha_0 \cdot L = 10^{-2}$. With these numbers we obtain, using (2.65) an improvement factor of 1.2×10^4 .

An important source of noise is the interference noise caused by the superposition of the signal wave with that part of the pump wave that is backscattered from the windows of the sample cell. Since the optical paths of the two waves through air differ considerably, every fluctuation of the air density causes a corresponding fluctuation in the phase difference between the two coherent waves, which results in the addition of random fluctuations to the signal amplitude monitored by the detector. Even without air fluctuations, periodic changes in this interference amplitude occur when the wavelength is tuned through the spectral range of interest.

This noise and the periodic false signals can be greatly reduced by implementing a fast periodic phase shift of the pump which averages over the fluctuations. To achieve this, the mirror M_2 in Fig. 2.22 reflecting the pump beam into the sample cell is mounted on a piezo element which periodically shifts the pathlength and with it the phase of the pump wave by $\Delta\varphi > 2\pi$ when an ac voltage with a frequency f is applied to the piezo. If f is large compared to the lock-in frequency, the lock-in averages out all phase fluctuations.

2.4.5 Advantages of Polarization Spectroscopy

Let us briefly summarize the advantages of polarization spectroscopy, discussed in the previous sections:

- Along with the other sub-Doppler techniques, it has the advantage of high spectral resolution, which is mainly limited by the residual Doppler width due to the finite angle between the pump beam and the probe beam. This limitation corresponds to that imposed to linear spectroscopy in collimated molecular beams by

the divergence angle of the molecular beam. The transit-time broadening can be reduced if the pump and probe beams are less tightly focused.

- The sensitivity is 2–3 orders of magnitude larger than that of saturation spectroscopy. It is surpassed only by that of the intermodulated fluorescence technique at very low sample pressures (Sect. 2.3.1).
- The possibility of distinguishing between P, R, and Q-lines is a particular advantage for the assignment of complex molecular spectra.
- The dispersion profile of the polarization signals allows a stabilization of the laser frequency to the line center without any frequency modulation. The large achievable signal-to-noise ratio assures an excellent frequency stability.

Meanwhile polarization spectroscopy has been applied to the measurement of many high-resolution atomic and molecular spectra. Examples can be found in [204, 230–236].

2.5 Multiphoton Spectroscopy

In this section we consider the simultaneous absorption of two or more photons by a molecule that undergoes a transition $E_i \rightarrow E_f$ with $(E_f - E_i) = \hbar \sum_i \omega_i$. The photons may either come from a single laser beam passing through the absorbing sample or they may be provided by two or more beams emitted from one or several lasers.

The first detailed theoretical treatment of two-photon processes was given in 1929 by Göppert-Mayer [237], but the experimental realization had to wait for the development of sufficiently intense light sources, now provided by lasers [238, 239].

2.5.1 Two-Photon Absorption

Two-photon absorption can be formally described by a two-step process from the initial level $|i\rangle$ via a “virtual level” $|v\rangle$ to the final level $|f\rangle$ (Fig. 2.30b). This fictitious virtual level is represented by a linear combination of the wave functions of all real molecular levels $|k_n\rangle$ that combine with $|i\rangle$ and $|f\rangle$ by allowed one-photon transitions. The excitation of $|v\rangle$ is equivalent to the sum of all off-resonance excitations of these real levels $|k_n\rangle$. The probability amplitude for a transition $|i\rangle \rightarrow |v\rangle$ is then represented by the sum of the amplitudes of all allowed transitions $|i\rangle \rightarrow |k\rangle$ with off-resonance detuning $(\omega - \omega_{ik})$. The same arguments hold for the second step $|v\rangle \rightarrow |f\rangle$.

For a molecule moving with a velocity \mathbf{v} , the probability A_{if} for a two-photon transition between the ground state E_i and an excited state E_f induced by the photons $\hbar\omega_1$ and $\hbar\omega_2$ from two light waves with the wave vectors $\mathbf{k}_1, \mathbf{k}_2$, the polariza-

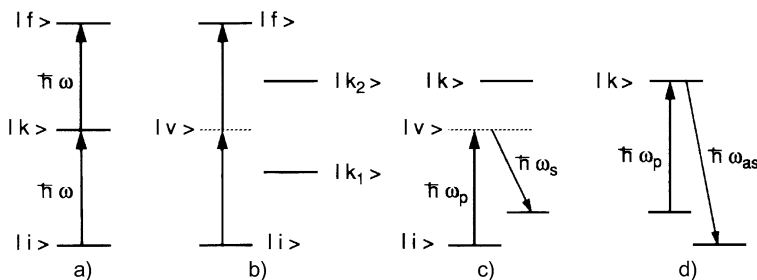


Fig. 2.30 Level schemes of different two-photon transitions: (a) resonant two-photon absorption with a real intermediate level $|k\rangle$; (b) nonresonant two-photon absorption with a virtual level $|v\rangle$; (c) Raman transition; (d) resonant anti-Stokes Raman scattering

tion unit vectors \hat{e}_1, \hat{e}_2 , and the intensities I_1, I_2 can be written as

$$A_{if} \propto \frac{\gamma_{if} I_1 I_2}{[\omega_{if} - \omega_1 - \omega_2 - \mathbf{v} \cdot (\mathbf{k}_1 + \mathbf{k}_2)]^2 + (\gamma_{if}/2)^2} \times \left| \sum_k \frac{\mathbf{D}_{ik} \cdot \hat{e}_1 \cdot \mathbf{D}_{kf} \cdot \hat{e}_2}{\omega_{ki} - \omega_1 - \mathbf{v} \cdot \mathbf{k}_1} + \frac{\mathbf{D}_{ik} \cdot \hat{e}_2 \cdot \mathbf{D}_{kf} \cdot \hat{e}_1}{\omega_{ki} - \omega_2 - \mathbf{v} \cdot \mathbf{k}_2} \right|^2. \quad (2.66)$$

The first factor gives the spectral line profile of the two-photon transition of a single molecule. It corresponds exactly to that of a single-photon transition of a moving molecule at the center frequency $\omega_{if} = \omega_1 + \omega_2 + \mathbf{v} \cdot (\mathbf{k}_1 + \mathbf{k}_2)$ with a homogeneous linewidth γ_{if} (Vol. 1, Sects. 3.1, 3.6). Integration over all molecular velocities \mathbf{v} gives a *Voigt profile* with a halfwidth that depends on the relative orientations of \mathbf{k}_1 and \mathbf{k}_2 . If both light waves are parallel, the Doppler width, which is proportional to $|\mathbf{k}_1 + \mathbf{k}_2|$, becomes maximum and is, in general, large compared to the homogeneous width γ_{if} . For $\mathbf{k}_1 = -\mathbf{k}_2$ the Doppler broadening vanishes and we obtain a pure Lorentzian line profile with a homogeneous linewidth γ_{if} provided that the laser linewidth is small compared to γ_{if} . This *Doppler-free two-photon spectroscopy* is discussed in Sect. 2.5.2.

Because the transition probability (2.66) is proportional to the product of the intensities $I_1 I_2$ (which has to be replaced by I^2 in the case of a single laser beam), *pulsed* lasers, which deliver sufficiently large peak powers, are generally used. The spectral linewidth of these lasers is often comparable to or even larger than the Doppler width. For nonresonant transitions $|\omega_{ki} - \omega_i| \gg \mathbf{v} \cdot \mathbf{k}_i$, and the denominators $(\omega_{ki} - \omega - \mathbf{k} \cdot \mathbf{v})$ in the sum in (2.66) can then be approximated by $(\omega_{ki} - \omega_i)$.

The second factor in (2.66) describes the transition probability for the two-photon transition. It can be derived quantum mechanically by second-order perturbation theory (see, for example, [240, 241]). This factor contains a sum of products of matrix elements $\mathbf{D}_{ik} \mathbf{D}_{kf}$ for the transitions between the initial level i and intermediate molecular levels k or between these levels k and the final state f , see Vol. 1, (2.110). The summation extends over all molecular levels k that are accessible by allowed one-photon transitions from the initial state $|i\rangle$. The denominator shows, however,

that only those levels k that are not too far off resonance with one of the Doppler-shifted laser frequencies $\omega'_n = \omega_n - \mathbf{v} \cdot \mathbf{k}_n$ ($n = 1, 2$) will mainly contribute.

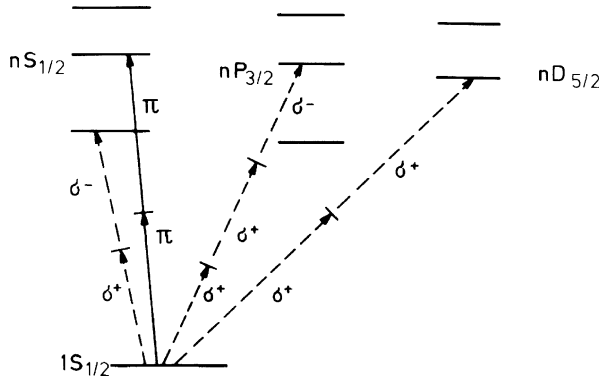
Often the frequencies ω_1 and ω_2 can be selected in such a way that the virtual level is close to a real molecular eigenstate, which greatly enhances the transition probability. It is therefore generally advantageous to excite the final level E_f by two different photons with $\omega_1 + \omega_2 = (E_f - E_i)/\hbar$ rather than by two photons out of the same laser with $2\omega = (E_f - E_i)/\hbar$.

The second factor in (2.66) describes quite generally the transition probability for all possible two-photon transitions such as Raman scattering or two-photon absorption and emission. Figure 2.30 illustrates schematically three different two-photon processes. The *important point is that the same selection rules are valid for all these two-photon processes*. Equation (2.66) reveals that both matrix elements \mathbf{D}_{ik} and \mathbf{D}_{kf} must be nonzero to give a nonvanishing transition probability A_{if} . This means that two-photon transitions can only be observed between two states $|i\rangle$ and $|f\rangle$ that are both connected to intermediate levels $|k\rangle$ by allowed single-photon optical transitions. Because the selection rule for single-photon transitions demands that the levels $|i\rangle$ and $|k\rangle$ or $|k\rangle$ and $|f\rangle$ have opposite parity, *the two levels $|i\rangle$ and $|f\rangle$ connected by a two-photon transition must have the same parity*. In atomic two-photon spectroscopy $s \rightarrow s$ or $s \rightarrow d$ transitions are allowed, and in diatomic homonuclear molecules $\Sigma_g \rightarrow \Sigma_g$ transitions are allowed.

It is therefore possible to reach molecular states that cannot be populated by single-photon transitions from the ground state. In this regard two-photon absorption spectroscopy is complementary to one-photon absorption spectroscopy, and its results are of particular interest because they yield information about states, which often had not been found before [242]. Often excited molecular states that are accessible from the ground state by one-photon transitions are perturbed by nearby states of opposite parity, which cannot be directly observed by one-photon spectroscopy. It is generally difficult to deduce the structure of these perturbing states from the degree of perturbations, while two-photon spectroscopy allows direct access to such states.

Since the matrix elements $\mathbf{D}_{ik} \cdot \hat{\mathbf{e}}_1$ and $\mathbf{D}_{kf} \cdot \hat{\mathbf{e}}_2$ depend on the polarization characteristics of the incident radiation, it is possible to select the accessible upper states by a proper choice of the polarization. While for single-photon transitions the total transition probability (summed over all M sublevels) is *independent* of the polarization of the incident radiation, there is a distinct polarization effect in multiphoton transitions, which can be understood by applying known selection rules to the two matrix elements in (2.66). For example, two parallel laser beams, which both have right-hand circular polarization, induce two-photon transitions in atoms with $\Delta L = 2$. This allows, for instance, $s \rightarrow d$ transitions, but not $s \rightarrow s$ transitions. When a circularly polarized wave is reflected back on itself, the right-hand circular polarization changes into a left-hand one, and if a two-photon transition is induced by one photon from each wave, only $\Delta L = 0$ transitions are selected which means that now $s \rightarrow s$ transitions are allowed but not $s \rightarrow d$ transitions. Figure 2.31 illustrates the different atomic transitions that are possible by multiphoton absorption of linearly polarized light and of right or left circularly polarized light.

Fig. 2.31 Different two-photon transitions in an atom, depending on the polarization characteristics \hat{e}_1 and \hat{e}_2 of the two laser fields



Different upper states can therefore be selected by a proper choice of the polarization. In many cases it is possible to gain information about the symmetry properties of the upper states from the known symmetry of the ground state and the polarization of the two light waves. Since the selection rules of two-photon absorption and Raman transitions are identical, one can utilize the group-theoretical techniques originally developed for Raman scattering to analyze the symmetry properties of excited states reached by the different two-photon techniques [243, 244].

2.5.2 Doppler-Free Multiphoton Spectroscopy

In the methods discussed in Sects. 2.3 and 2.4, the Doppler width had been reduced or even completely eliminated by proper selection of a *velocity subgroup* of molecules with the velocity components $v_z = 0 \pm \Delta v_z$, due to selective saturation. The technique of Doppler-free multiphoton spectroscopy does not need such a velocity selection because *all* molecules in the absorbing state, regardless of their velocities, can contribute to the Doppler-free transition. Therefore the sensitivity of Doppler-free multiphoton spectroscopy is comparable to that of saturation spectroscopy in spite of the smaller transition probabilities.

While the general concepts and the transition probability of multiphoton transitions were discussed in Sect. 2.5.1, we concentrate in this subsection on *Doppler-free* multiphoton spectroscopy [245–249].

Assume a molecule moves with a velocity \mathbf{v} in the laboratory frame. In the reference frame of the moving molecule the frequency ω of an EM wave with the wave vector \mathbf{k} is Doppler shifted to (Vol. 1, Sect. 3.2)

$$\omega' = \omega - \mathbf{k} \cdot \mathbf{v}. \quad (2.67)$$

The resonance condition for the simultaneous absorption of two photons is

$$(E_f - E_i)/\hbar = (\omega'_1 + \omega'_2) = \omega_1 + \omega_2 - \mathbf{v} \cdot (\mathbf{k}_1 + \mathbf{k}_2). \quad (2.68)$$

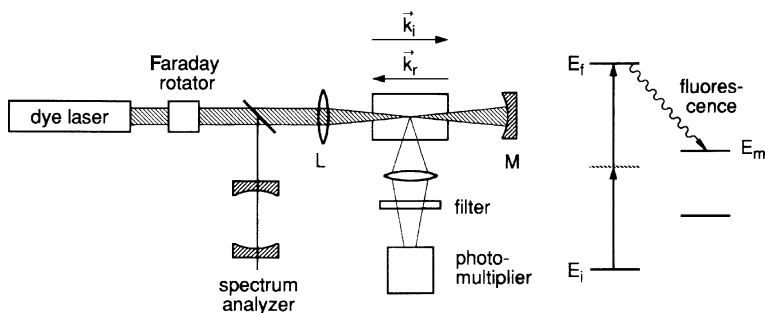


Fig. 2.32 Experimental arrangement for Doppler-free two-photon spectroscopy

If the two photons are absorbed out of two light waves with equal frequencies $\omega_1 = \omega_2 = \omega$, which travel in opposite directions, we obtain $\mathbf{k}_1 = -\mathbf{k}_2$ and (2.68) shows that the Doppler shift of the two-photon transition becomes zero. This means that *all* molecules, *independent of their velocities*, absorb at the same sum frequency $\omega_1 + \omega_2 = 2\omega$.

Although the probability of a two-photon transition is generally much lower than that of a single-photon transition, the fact that *all* molecules in the absorbing state can contribute to the signal may outweigh the lower transition probability, and the signal amplitude may even become, in favorable cases, larger than that of the saturation signals.

The considerations above can be generalized to many photons. When the moving molecule is simultaneously interacting with several plane waves with wave vectors \mathbf{k}_i and one photon is absorbed from each wave, the total Doppler shift $\mathbf{v} \cdot \sum_i \mathbf{k}_i$ becomes zero for $\sum \mathbf{k}_i = 0$.

Figure 2.32 shows a possible experimental arrangement for the observation of Doppler-free two-photon absorption. The two oppositely traveling waves are formed by reflection of the output beam from a single-mode tunable dye laser. The Faraday rotator prevents feedback into the laser. The two-photon absorption is monitored by the fluorescence emitted from the final state E_f into other states E_m . From (2.66) it follows that the probability of two-photon absorption is proportional to the square I^2 of the laser intensity. Therefore, the two beams are focused into the sample cell by the lens L and the spherical mirror M.

For illustration the examples in Fig. 2.33 show the Doppler-free two-photon spectra of the $3S \rightarrow 5S$ transition in the sodium atom with resolved hyperfine structure [245].

The line profile of two-photon transitions can be deduced from the following consideration: assume the reflected beam in Fig. 2.32 to have the same intensity as the incident beam. In this case the two terms in the second factor of (2.66) become identical, while the first factor, which describes the line profile, differs for the case when both photons are absorbed out of the same beam from the case when they come from different beams. The probability for the latter case is twice as large as for the former case. This can be seen as follows: Let (a, a) be the probability for the

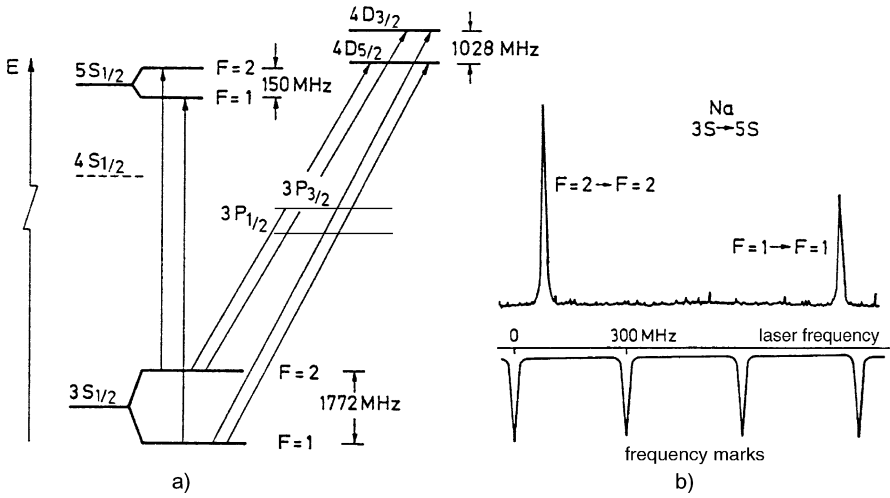


Fig. 2.33 Doppler-free two-photon spectrum of the Na atom: (a) level scheme of the $3S \rightarrow 5S$ and $3S \rightarrow 4D$ transitions; (b) $3S \rightarrow 5S$ transition for $\Delta F = 0$ with resolved hyperfine structure [245]

case that both photons are provided by the incident beam and (b, b) by the reflected beam. The total probability for a two-photon absorption with both photons of the same beam (which gives a Doppler-broadened contribution to the signal) is then $(a, a)^2 + (b, b)^2$.

The probability amplitude of the Doppler-free absorption is the sum $(a, b) + (b, a)$ of two nondistinguishable events. The total probability for this case is then $|(a, b) + (b, a)|^2$. For equal intensities of the two beams this is twice the probability $(a, a)^2 + (b, b)^2$.

We therefore obtain from (2.66) for the two-photon absorption probability

$$\begin{aligned}
 W_{if} \propto & \left| \sum_m \frac{(\mathbf{D}_{im} \hat{\mathbf{e}}_1)(\mathbf{D}_{mf} \hat{\mathbf{e}}_2)}{\omega - \omega_{im} - \mathbf{k}_1 \cdot \mathbf{v}} + \sum_m \frac{(\mathbf{D}_{im} \hat{\mathbf{e}}_2)(\mathbf{D}_{mf} \hat{\mathbf{e}}_1)}{\omega - \omega_{im} - \mathbf{k}_2 \cdot \mathbf{v}} \right|^2 I^2 \\
 & \times \left[\frac{4\gamma_{if}}{(\omega_{if} - 2\omega)^2 + (\gamma_{if}/2)^2} + \frac{\gamma_{if}}{(\omega_{if} - 2\omega - 2\mathbf{k} \cdot \mathbf{v})^2 + (\gamma_{if}/2)^2} \right. \\
 & \left. + \frac{\gamma_{if}}{(\omega_{if} - 2\omega + 2\mathbf{k} \cdot \mathbf{v})^2 + (\gamma_{if}/2)^2} \right]. \quad (2.69)
 \end{aligned}$$

Integration over the velocity distribution yields the absorption profile

$$\begin{aligned}
 \alpha(\omega) \propto & \Delta N^0 I^2 \left| \sum_m \frac{(\mathbf{D}_{im} \hat{\mathbf{e}})(\mathbf{D}_{mf} \hat{\mathbf{e}})}{\omega - \omega_{im}} \right|^2 \\
 & \times \left\{ \exp \left[- \left(\frac{\omega_{if} - 2\omega}{2kv_p} \right)^2 \right] + \frac{kv_p}{\sqrt{\pi}} \frac{\gamma_{if}/2}{(\omega_{if} - 2\omega)^2 + (\gamma_{if}/2)^2} \right\}, \quad (2.70)
 \end{aligned}$$

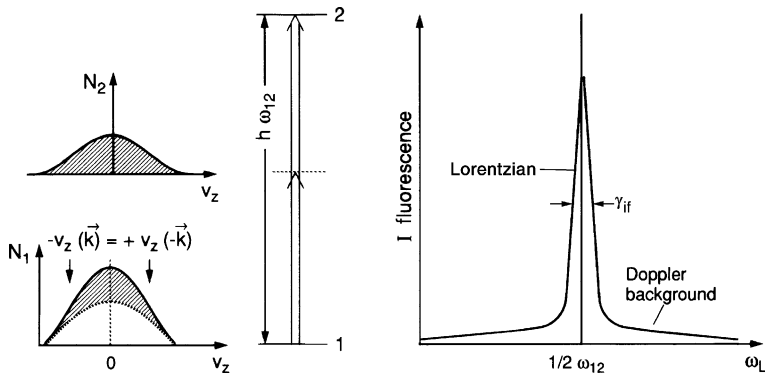


Fig. 2.34 Schematic line profile of a Doppler-free two-photon signal with (greatly exaggerated) Doppler-broadened background

where $v_p = (2kT/m)^{1/2}$ is the most probable velocity, and $\Delta N_0 = N_i^0 - N_f$ the nonsaturated population difference. The absorption profile (2.70) represents a superposition of a Doppler-broadened background and a narrow Lorentzian profile with the linewidth $\gamma_{if} = \gamma_i + \gamma_f$ (Fig. 2.34).

As was shown above, the area under the Doppler profile with halfwidth $\Delta\omega_D$ is half of that under the narrow Lorentzian profile with halfwidth γ_{if} . However, due to its larger linewidth its peak intensity amounts only to the fraction

$$\epsilon = \frac{\gamma_{if}\sqrt{\pi}}{2kv_p} \simeq \frac{\gamma_{if}}{2\Delta\omega_D},$$

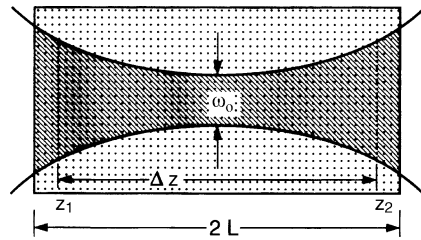
of the Lorentzian peak heights.

Example 2.10 With $\gamma_{if} = 20$ MHz, $\Delta\omega_D = 2$ GHz, the Doppler-free signal in Fig. 2.34 is about 200 times higher than the maximum of the Doppler-broadened background.

By choosing the proper polarization of the two laser waves, the background can often be completely suppressed. For example, if the incident laser beam has σ^+ polarization, a $\lambda/4$ -plate between mirror M and the sample in Fig. 2.32 converts the reflected beam to σ^- polarization. Two-photon absorption on a $S \rightarrow S$ transition with $\Delta M = 0$ is then possible only if one photon comes from the incident wave and the other from the reflected wave because two photons out of the same beam would induce transitions with $\Delta M = \pm 2$.

For the resonance case $2\omega = \omega_{if}$, the second term in (2.69) becomes $2kv_p/(\gamma_{if}\sqrt{\pi}) \gg 1$. We can neglect the contribution of the Doppler term and obtain the

Fig. 2.35 Beam waist w_0 and Rayleigh length L for optimum focusing in two-photon spectroscopy



maximum two-photon absorption:

$$\alpha\left(\omega = \frac{1}{2}\omega_{if}\right) \propto I^2 \frac{\Delta N^0 k v_p}{\sqrt{\pi} \gamma_{if}} \left| \sum_m \frac{(\mathbf{D}_{im} \cdot \hat{\mathbf{e}}) \cdot (\mathbf{D}_{mf} \cdot \hat{\mathbf{e}})}{\omega - \omega_{im}} \right|^2. \quad (2.71)$$

Note Although the product of matrix elements in (2.71) is generally much smaller than the corresponding one-photon matrix elements, the magnitude of the Doppler-free two-photon signal (2.68) may exceed that of Doppler-free saturation signals. This is due to the fact that *all* molecules in level $|i\rangle$ contribute to two-photon absorption, whereas the signal in Doppler-free saturation spectroscopy is provided only by the subgroup of molecules out of a narrow velocity interval $\Delta v_z = 0 \pm \gamma/k$. For $\gamma = 0.01 \Delta \omega_D$, this subgroup represents only about 1 % of all molecules.

For *molecular* transitions the matrix elements D_{im} and D_{mf} are composed of three factors: the electronic transition dipole element, the Franck–Condon factor, and the Hönl–London factor (Sect. 1.7). Within the two-photon dipole approximation $\alpha(\omega)$ becomes zero if one of these factors is zero. The calculation of linestrengths for two- or three-photon transitions in diatomic molecules can be found in [243, 244].

2.5.3 Influence of Focusing on the Magnitude of Two-Photon Signals

Since the two-photon absorption probability is proportional to the square of the incident laser intensity, the signal can generally be increased by focusing the laser beam into the sample cell. However, the signal is also proportional to the number of absorbing molecules within the interaction volume, which decreases with decreasing focal volume. With pulsed lasers the two-photon transition may already be saturated at a certain incident intensity without focusing. In this case focusing will decrease the signal. The optimization of the focusing conditions can be based on the following estimation: Assume the laser beams propagate into the $\pm z$ -directions. The two-photon absorption is monitored via the fluorescence from the upper level $|f\rangle$ and can be collected from a sample volume $V = \pi \cdot \int_{z_1}^{z_2} r^2(z) dz$ (Fig. 2.35), where

$r(z)$ is the beam radius (Vol. 1, Sect. 5.3) and Δz the maximum length of the interaction volume seen by the collecting optics. The two-photon signal is then for $N_f \ll N_i$, that is, $\Delta N \approx N_i$, according to (2.71)

$$S\left(\frac{1}{2}\omega_{if}\right) \propto N_i \left| \sum_m \frac{(D_{im}\hat{\mathbf{e}}) \cdot (D_{mf}\hat{\mathbf{e}})}{\omega - \omega_{im}} \right|^2 \int_z \int_r I^2(r, z) 2\pi r \, dr \, dz, \quad (2.72)$$

where N_i is the density of the molecules in the absorbing level $|i\rangle$ and

$$I(r, z) = \frac{2P_0}{\pi w^2} e^{-2r^2/w^2} \quad (2.73)$$

gives the radial intensity distribution of the laser beam with power P_0 in the TEM₀₀ mode with a Gaussian intensity profile. The beam waist

$$w(z) = w_0 \sqrt{1 + \frac{\lambda z}{\pi w_0^2}}, \quad (2.74)$$

gives the radius of the Gaussian beam in the vicinity of the focus at $z = 0$ (Vol. 1, Sect. 5.4). The Rayleigh length $L = \pi w_0^2/\lambda$ gives that distance from the focus at $z = 0$ where the beam cross section $\pi w^2(L) = 2\pi w_0^2$ has increased by a factor of two compared to the area πw_0^2 at $z = 0$.

Inserting (2.73, 2.74) into (2.72) shows that the signal S_{if} is proportional to

$$S_{if} \propto \int_0^\infty \int_{z_1}^{z_2} \frac{1}{w^4} e^{-4r^2/w^2} r \, dr \, dz = 4 \int_{z_1}^{z_2} \frac{dz}{w^2}. \quad (2.75a)$$

S_{if} becomes maximum if the integral

$$\int_{-\Delta z/2}^{+\Delta z/2} \frac{dz}{1 + (\lambda z/\pi w_0^2)^2} = 2L \arctan[\Delta z/(2L)], \quad (2.75b)$$

with $\Delta z = z_2 - z_1$ has a maximum value. Equation (2.75a–2.75b) shows that the signal cannot be increased any longer by stronger focusing when the Rayleigh length L becomes smaller than the interval Δz from which the fluorescence can be collected.

The two-photon signal can be greatly enhanced if the sample is placed either inside the laser resonator or in an external resonator, which has to be tuned synchronously with the laser wavelength (Sect. 1.4).

2.5.4 Examples of Doppler-Free Two-Photon Spectroscopy

The first experiments on Doppler-free two-photon spectroscopy were performed on the alkali atoms [245–249] because their two-photon transitions can be induced by

Fig. 2.36 Measurement of the isotope shift of the stable lead isotopes measured with Doppler-free two-photon spectroscopy at $\lambda_{\text{exc}} = 450 \text{ nm}$ and monitored via fluorescence [250]

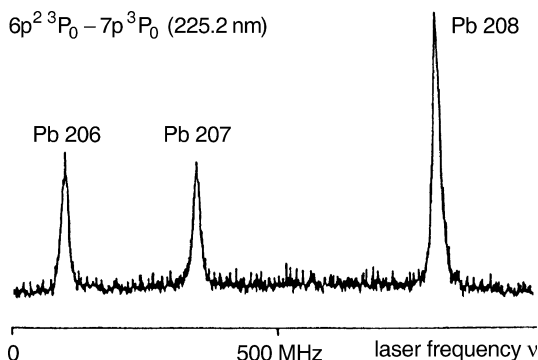
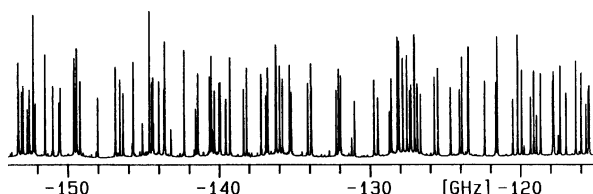


Fig. 2.37 Section of the Doppler-free two-photon excitation spectrum of the 14_0^1Q_0 band of C_6H_6 [255]



cw dye lasers or diode lasers in convenient spectral ranges. Furthermore, the first excited P state is not too far away from the virtual level in Fig. 2.30b. This enlarges the two-photon transition probabilities for such “near-resonant” transitions. Meanwhile, there are numerous further applications of this sub-Doppler technique in atomic and molecular physics. We shall illustrate them by a few examples only.

The isotope shift between different stable lead isotopes shown in Fig. 2.36 has been determined by Doppler-free two-photon absorption of a cw dye laser beam at $\lambda = 450.4 \text{ nm}$ on the transition $6p^2\ ^3P_0 \rightarrow 7p\ ^3P_0$ [250] using the experimental arrangement of Fig. 2.32.

Doppler-free two-photon transitions to atomic Rydberg levels [251] allow the accurate determination of quantum defects and of level shifts in external fields. Hyperfine structures in Rydberg states of two-electron atoms, such as calcium and singlet–triplet mixing of the valence state $4s$ and 1D and 3D Rydberg levels have been thoroughly studied by Doppler-free two-photon spectroscopy [252].

The application of two-photon spectroscopy to molecules has brought a wealth of new insight to excited molecular states. One example is the two-photon excitation of CO in the fourth positive system $A\ ^1\Pi \leftarrow X\ ^1\Sigma_g$ and of N_2 in the Lyman–Birge–Hopfield system with a narrow-band pulsed frequency-doubled dye laser. Doppler-free spectra of states with excitation energies between 8–12 eV can be measured with this technique [253].

For larger molecules, rotationally resolved absorption spectra could, for the first time, be measured, as has been demonstrated for the UV spectra of benzene C_6H_6 . Spectral features, which had been regarded as true continua in former times, could now be completely resolved (Fig. 2.37) and turned out to be dense but discrete rotational-line spectra [254, 255]. The lifetimes of the upper levels could be determined from the natural linewidths of these transitions [256]. It was proven that

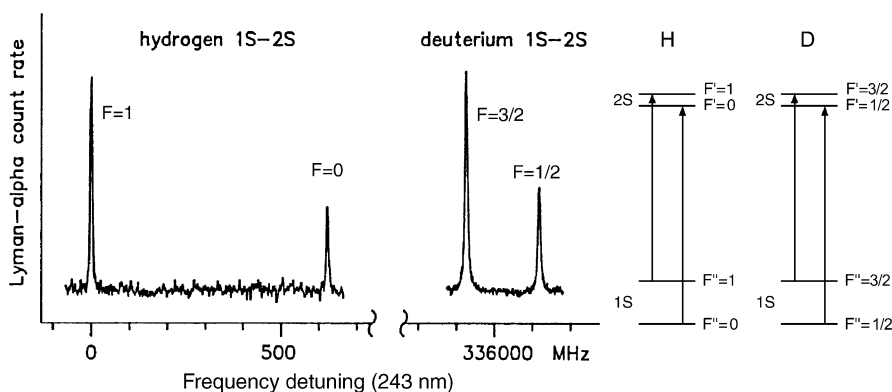


Fig. 2.38 Doppler-free two-photon transitions of hydrogen 1S–2S and deuterium 1S–2S [260]. For each of the two photons from opposite laser beams, only transitions with $\Delta F = 0$ are allowed

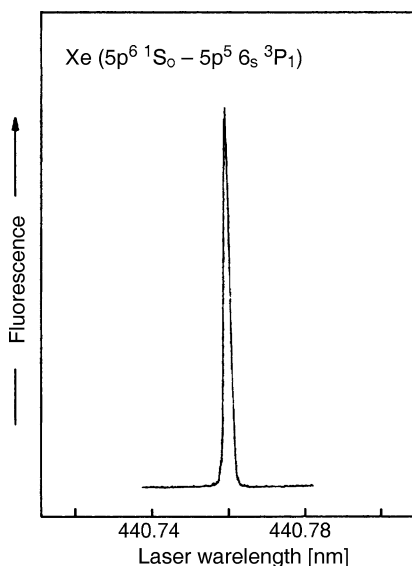
these lifetimes strongly decrease with increasing vibrational–rotational energy in the excited electronic state because of the increasing rate of radiationless transitions [257].

Molecular two-photon spectroscopy can also be applied in the infrared region to induce transitions between rotational–vibrational levels within the electronic ground state. One example is the Doppler-free spectroscopy of rotational lines in the ν_2 vibrational bands of NH_3 [258]. This allows the study of the collisional properties of the ν_2 vibrational manifold from pressure broadening and shifts (Vol. 1, Sect. 3.3) and Stark shifts.

Near-resonant two-photon spectroscopy of NH_3 has been reported by Winnewisser et al. [259]. Using a tunable diode laser with frequency ν_1 the two-photon excitation $\nu_1 + \nu_2$ of the $2\nu_2$ (1, 1) level of NH_3 was observed with the second photon $h\nu_2$ coming from a fixed-frequency CO_2 laser.

The possibilities of Doppler-free two-photon spectroscopy for metrology and fundamental physics has been impressively demonstrated by precision measurements of the 1S–2S transition in atomic hydrogen [260–263]. Precise measurements of this one-photon forbidden transition with a very narrow natural linewidth of 1.3 Hz yield accurate values of fundamental constants and can provide stringent tests of quantum electrodynamic theory (Sect. 9.7). A comparison of the 1S–2S transition frequency with the 2S–3P frequency allows the precise determination of the Lamb shift of the 1S ground state [261], whereas the 2S Lamb shift was already measured long ago by the famous Lamb–Rutherford experiments where the RF transition between $2S_{1/2}$ and $2P_{1/2}$ were observed. Because of the isotope shift the 1S–2S transitions of ^1H and $^2\text{H} = {}^2\text{D}$ differ by $2 \times 335.49716732 \text{ GHz} = 670.99433464 \text{ GHz}$ (Fig. 2.38). From this measurement a value $r_D^2 - r_P^2 = 3.8212 \text{ fm}^2$ for the difference of the mean square charge radii of proton and deuteron is derived. The Rydberg constant has been determined within a relative uncertainty of 10^{-10} [262–264]. The attainable precision allows a test of the limits of quantum-electrodynamics. Of particular interest is the questions

Fig. 2.40 Three-photon excited resonance fluorescence in Xe at $\lambda = 147$ nm, excited with a pulsed dye laser at $\lambda = 440.76$ nm with 80 kW peak power. The Xe pressure was 8 mtorr [265]



The three-photon absorption can be used for the excitation of high-lying molecular levels with the same parity as accessible to one-photon transitions. However, for a one-photon absorption, lasers with a wavelength $\lambda/3$ have to be available in order to reach the same excitation energy. An example of Doppler-limited collinear three-photon spectroscopy is the excitation of high-lying levels of xenon and CO with a narrow-band pulsed dye laser at $\lambda = 440$ nm (Fig. 2.40). For one-photon transitions light sources at $\lambda = 146.7$ nm in the VUV would have been necessary.

In the case of *Doppler-free* multiphoton absorption, momentum conservation

$$\sum_k \mathbf{p}_k = \hbar \sum_k \mathbf{k}_k = 0, \quad (2.76)$$

has to be fulfilled in addition to energy conservation $\sum \hbar \omega_k = E_f - E_i$. Each of the absorbed photons transfers the momentum $\hbar \mathbf{k}_k$ to the molecule. If (2.76) holds, the total transfer of momentum is zero, which implies that the velocity of the absorbing molecule has not changed. This means that the photon energy $\hbar \sum \omega_k$ is completely converted into excitation energy of the molecule without changing its kinetic energy. This is independent of the initial velocity of the molecule, that is, the transition is Doppler-free.

A possible experimental arrangement for Doppler-free three-photon absorption spectroscopy is depicted in Fig. 2.41. The three laser beams generated by beam splitting of a single dye laser beam cross each other under 120° in the absorbing sample.

The absorption probability increases if a two-photon resonance can be found. One example is illustrated in Fig. 2.42a, where the $4D$ level of the Na atom is excited by two-photons of a dye laser at $\lambda = 578.7$ nm and further excitation by a third photon reaching high-lying Rydberg levels nP or nF with the electronic orbital

Fig. 2.41 Possible arrangements for Doppler-free three-photon spectroscopy

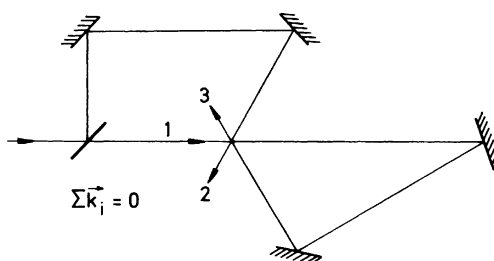
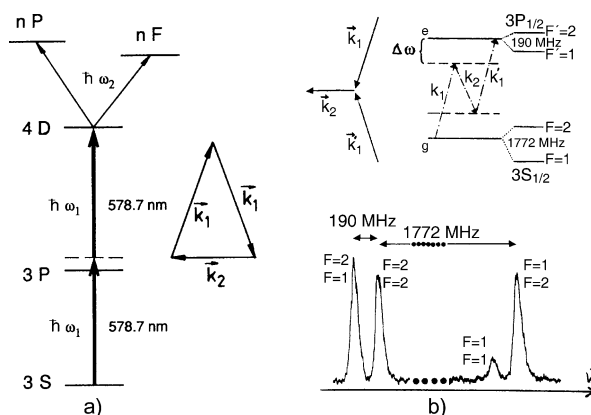


Fig. 2.42 Level schemes for Doppler-free three-photon spectroscopy of the Na atom: (a) stepwise excitation of Rydberg states; (b) Raman-type process shown for the example of the $3S-3P$ excitation of the Na atom. Laser 1 is tuned while L2 is kept 30 GHz below the Na D_1 line [266]



momentum $\ell = 1$ or $\ell = 3$. For Doppler-free excitation the wave-vector diagram of Fig. 2.41 has been used [266].

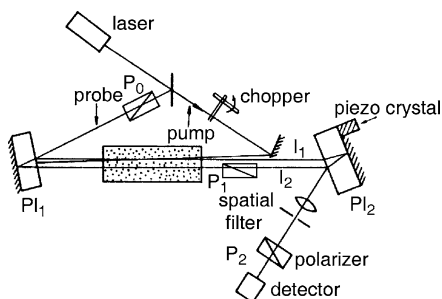
Three-photon excitation may also be used for a Raman-type process, depicted in Fig. 2.42b, which proceeds via two virtual levels. This Doppler-free technique was demonstrated for the $3^2S_{1/2} \rightarrow 3^2P_{1/2}$ transition of the Na atom, where the photons with the momentum $\hbar\mathbf{k}_1$ and $\hbar\mathbf{k}'_1$ are absorbed while the photon with the momentum $\hbar\mathbf{k}_2$ is emitted. The hyperfine structure of the upper and lower states could readily be resolved [266].

Multiphoton absorption of visible photons may result in ionization of atoms or molecules. At a given laser intensity the ion rate $N_{\text{ion}}(\lambda_L)$ recorded as a function of the laser intensity shows narrow maxima if one-, two-, or three-photon resonances occur. If, for instance, the ionization potential (IP) is smaller than $3\hbar\omega$, resonances in the ionization yield are observed, either when the laser frequency ω is in resonance with a two-photon transition between the levels $|i\rangle$ and $|f\rangle$, i.e. $(E_f - E_i = 2\hbar\omega)$, or when autoionizing Rydberg states can be reached by three-photon transitions [267].

Multiphoton absorption has also been observed on transitions within the electronic ground states of molecules, induced by infrared photons of a CO_2 laser [268, 269]. At sufficient intensities this multiphoton excitation of high vibrational-rotational states may lead to the dissociation of the molecule [270].

If the first step of the multiphoton excitation can be chosen isotope selectively so that a wanted isotopomer has a larger absorption probability than the other isotopomers of the molecular species, selective dissociation may be achieved [270],

Fig. 2.43 Schematic arrangement of saturated interference spectroscopy



which can be used for isotope separation by chemical reactions with the isotope-selective dissociation products (Sect. 10.2).

2.6 Special Techniques of Nonlinear Spectroscopy

In this section we will briefly discuss some variations of saturation, polarization, or multiphoton spectroscopy that either increase the sensitivity or are adapted to the solution of special spectroscopic problems. They are often based on combinations of several nonlinear techniques.

2.6.1 Saturated Interference Spectroscopy

The higher sensitivity of polarization spectroscopy compared with conventional saturation spectroscopy results from the detection of *phase differences* rather than amplitude differences. This advantage is also used in a method that monitors the interference between two probe beams where one of the beams suffers saturation-induced phase shifts. This saturated interference spectroscopy was independently developed in different laboratories [271, 272]. The basic principle can easily be understood from Fig. 2.43. We follow here the presentation in [271].

The probe beam is split by the plane-parallel plate PI1 into two beams. One beam passes through that region of the absorbing sample that is saturated by the pump beam; the other passes through an unsaturated region of the same sample cell. The two beams are recombined by a second plane-parallel plate PI2. The two carefully aligned parallel plates form a Jamin interferometer [273], which can be adjusted by a piezoelement in such a way that without the saturating pump beam the two probe waves with intensities I_1 and I_2 interfere destructively.

If the saturation by the pump wave introduces a phase shift φ , the resulting intensity at the detector becomes

$$I = I_1 + I_2 - 2\sqrt{I_1 I_2} \cos \varphi. \quad (2.77)$$

The intensities I_1 and I_2 of the two interfering probe waves can be made equal by placing a polarizer P1 into one of the beams and a second polarizer P2 in front of the detector. Due to a slight difference δ in the absorptions of the two beams by the sample molecules, their intensities at the detector are related by

$$I_1 = I_2(1 + \delta) \quad \text{with } \delta \ll 1.$$

For small phase shifts φ ($\varphi \ll 1 \rightarrow \cos \varphi \approx 1 - \frac{1}{2}\varphi^2$), we can approximate (2.77) by

$$I \approx \left(\frac{1}{4}\delta^2 + \varphi^2 \right) I_2, \quad (2.78)$$

when we neglect the higher-order terms $\delta\varphi^2$ and $\delta^2\varphi^2$. The amplitude difference δ and the phase shift φ are both caused by selective saturation of the sample through the monochromatic pump wave, which travels in the opposite direction. Analogous to the situation in polarization spectroscopy, we therefore obtain Lorentzian and dispersion profiles for the frequency dependence of both quantities

$$\delta(\omega) = \frac{\delta_0}{1 + x^2}, \quad \varphi(\omega) = \frac{1}{2}\delta_0 \frac{x}{1 + x^2}, \quad (2.79)$$

where $\delta_0 = \delta(\omega_0)$, $x = 2(\omega - \omega_0)/\gamma$, and γ is the homogeneous linewidth (FWHM).

Inserting (2.79) into (2.78) yields, for the total intensity I at the minimum of the interference patterns, the Lorentzian profile,

$$I = \frac{1}{4} \frac{I_2 \delta_0^2}{1 + x^2}. \quad (2.80)$$

According to (2.79), the phase differences $\varphi(\omega)$ depends on the laser frequency ω . However, it can always be adjusted to zero while the laser frequency is scanned. This can be accomplished by a sine-wave voltage at the piezoelement, which causes a modulation

$$\varphi(\omega) = \varphi_0(\omega) + a \sin(2\pi f_1 t).$$

When the detector signal is fed to a lock-in amplifier that is tuned to the modulation frequency f_1 , the lock-in output can drive a servo loop to bring the phase difference φ_0 back to zero. For $\varphi(\omega) \equiv 0$, we obtain from (2.78, 2.79)

$$I(\omega) = \frac{1}{4} \delta(\omega)^2 I_2 = \frac{1}{4} \frac{\delta_0^2 I_2}{(1 + x^2)^2}. \quad (2.81)$$

The halfwidth of this signal is reduced from γ to $(\sqrt{2} - 1)^{1/2} \gamma \approx 0.64\gamma$.

Contrary to the situation in polarization spectroscopy, where for slightly uncrossed polarizers the line shape of the polarization signal is a superposition of Lorentzian and dispersion profiles, with saturated interference spectroscopy pure Lorentzian profiles are obtained because the phase shift is compensated by the feedback control. Measuring the first derivative of the profiles, pure dispersion-type signals appear. To achieve this, the output of the lock-in amplifier that controls the

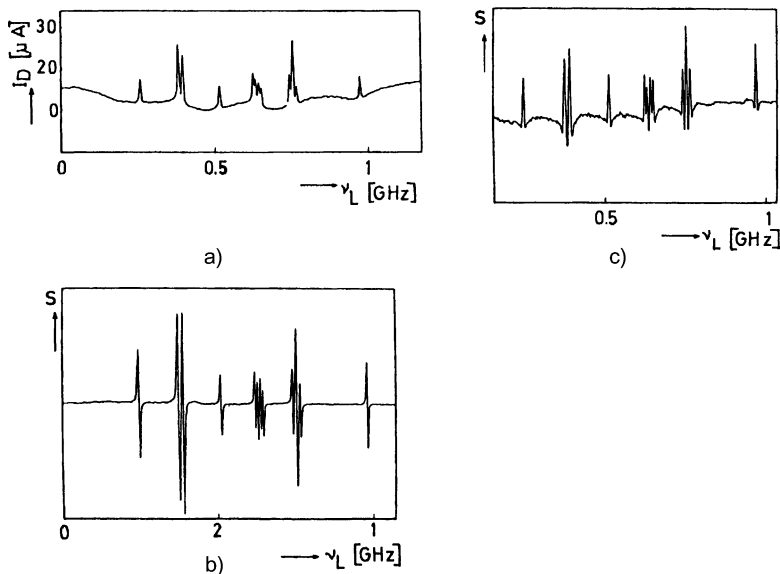


Fig. 2.44 Saturated interference spectra of I_2 at $\lambda = 600$ nm: (a) saturated absorption signal of the hfs components; (b) first-derivative spectrum of (a); (c) first derivative of saturated dispersion signal [272]

phase is fed into another lock-in that is tuned to a frequency f_2 ($f_2 \ll f_1$) at which the saturating pump beam is chopped.

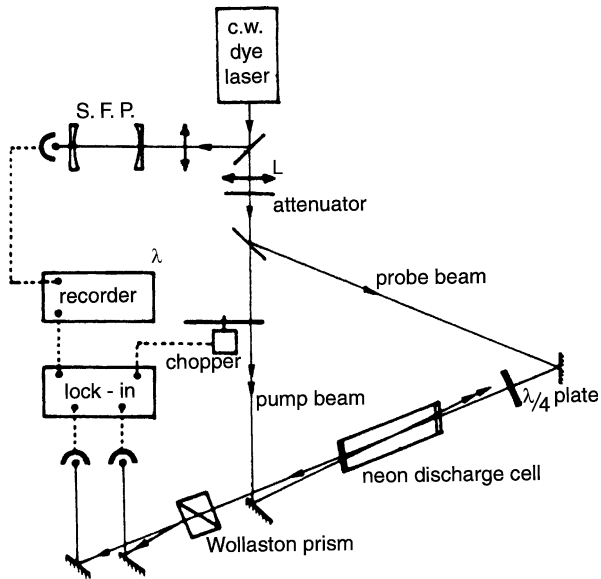
The method has been applied so far to the spectroscopy of Na_2 [271] and I_2 [272]. Figure 2.44a shows saturated absorption signals in I_2 obtained with conventional saturation spectroscopy using a dye laser at $\lambda = 600$ nm with 10 mW pump power and 1 mW probe power. Figure 2.44b displays the first derivative of the spectrum in Fig. 2.44a and Fig. 2.44c the first derivative of the saturated interference signal.

The sensitivity of the saturated interference technique is comparable to that of polarization spectroscopy. While the latter can be applied only to transitions from levels with a rotational quantum number $J \geq 1$, the former works also for $J = 0$. An experimental drawback may be the critical alignment of the Jamin interferometer and its stability during the measurements.

2.6.2 Doppler-Free Laser-Induced Dichroism and Birefringence

A slight modification of the experimental arrangement used for polarization spectroscopy allows the simultaneous observation of saturated absorption *and* dispersion [274]. While in the setup of Fig. 2.22 the probe beam had linear polarization, here a circularly polarized probe and a linearly polarized pump beam are used (Fig. 2.45). The probe beam can be composed of two components with linear polarization parallel and perpendicular to the pump beam polarization. Due to anisotropic saturation

Fig. 2.45 Experimental arrangement for observation of Doppler-free laser-induced dichroism and birefringence [274]



by the pump, the absorption coefficients α_{\parallel} and α_{\perp} and the refractive indices n_{\parallel} and n_{\perp} experienced by the probe beam are different for the parallel and the perpendicular polarizations. This causes a change of the probe beam polarization, which is monitored behind a linear analyzer rotated through the angle β from the reference direction π . Analogous to the derivation in Sect. 2.4.2, one can show that the transmitted intensity of a circularly polarized probe wave with incident intensity I is for $\alpha L \ll 1$ and $\Delta n(L/\lambda) \ll 1$

$$I_t(\beta) = \frac{I}{2} \left(1 - \frac{\alpha_{\parallel} + \alpha_{\perp}}{2} L - \frac{L}{2} \Delta \alpha \cos 2\beta - \frac{\omega L}{c} \Delta n \sin 2\beta \right), \quad (2.82)$$

with $\Delta \alpha = \alpha_{\parallel} - \alpha_{\perp}$ and $\Delta n = n_{\parallel} - n_{\perp}$.

The difference of the two transmitted intensities

$$\Delta_1 = I_t(\beta = 0^\circ) - I_t(\beta = 90^\circ) = IL\Delta\alpha/2, \quad (2.83)$$

gives the pure dichroism signal (anisotropic saturated absorption), while the difference

$$\Delta_2 = I_t(45^\circ) - I_t(-45^\circ) = I(\omega L/c)\Delta n, \quad (2.84)$$

yields the pure birefringence signal (saturated dispersion). A birefringent Wollaston prism behind the interaction region allows the spatial separation of the two probe beam components with mutually orthogonal polarizations. The two beams are monitored by two identical photodiodes. After a correct balance of the output signals, a differential amplifier records directly the desired differences Δ_1 and Δ_2 if the axes of the birefringent prism have suitable orientations.

Fig. 2.46 Comparison of different techniques for measuring the neon transition $1s_2-2p_2$ at $\lambda = 588.2$ nm: (a) intracavity saturation spectroscopy (Lamb peak of the laser output $I_L(\omega)$ with Doppler-broadened background); (b) laser-induced dichroism; and (c) laser-induced birefringence [274]

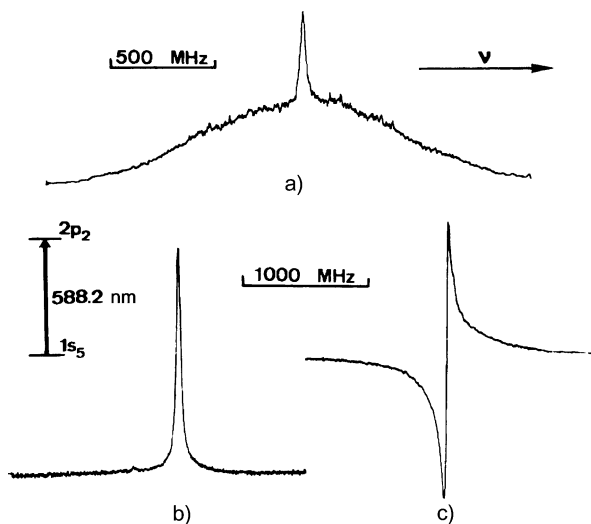


Figure 2.46 illustrates the advantages of this technique. The upper spectrum represents a Lamb peak in the intracavity saturation spectrum of the neon line ($1s \rightarrow 2p$) at $\lambda = 588.2$ nm (Sect. 2.3.3). Due to the collisional redistribution of the atomic velocities, a broad and rather intense background appears in addition to the narrow peak. This broad structure is not present in the dichroism and birefringent curves (Fig. 2.46b, c). This improves the signal-to-noise ratio and the spectral resolution.

2.6.3 Heterodyne Polarization Spectroscopy

In most detection schemes of saturation or polarization spectroscopy the intensity fluctuations of the probe laser represent the major contribution to the noise. Generally, the noise power spectrum $P_{\text{Noise}}(f)$ shows a frequency-dependence, where the spectral power density decreases with increasing frequency (e.g., $1/f$ -noise). It is therefore advantageous for a high S/N ratio to detect the signal S behind a lock-in amplifier at high frequencies f .

This is the basic idea of heterodyne polarization spectroscopy [275, 276], where the pump wave at the frequency ω_p passes through an acousto-optical modulator, driven at the modulation frequency f , which generates sidebands at $\omega = \omega_p \pm 2\pi f$ (Fig. 2.47). The sideband at $\omega_t = \omega_p + 2\pi f$ is sent as a pump beam through the sample cell, while the probe beam at frequency ω_p is split off the laser beam in front of the modulator. Otherwise the setup is similar to that of Fig. 2.22.

The signal intensity transmitted by the analyzer P_3 is described by (2.50). However, the quantity $x = 2(\omega - \omega_0 - 2\pi f)/\gamma$ now differs from (2.48) by the frequency shift f , and the amplitude of the polarization signal is modulated at the difference frequency f between pump and probe beam. The signal can therefore be detected

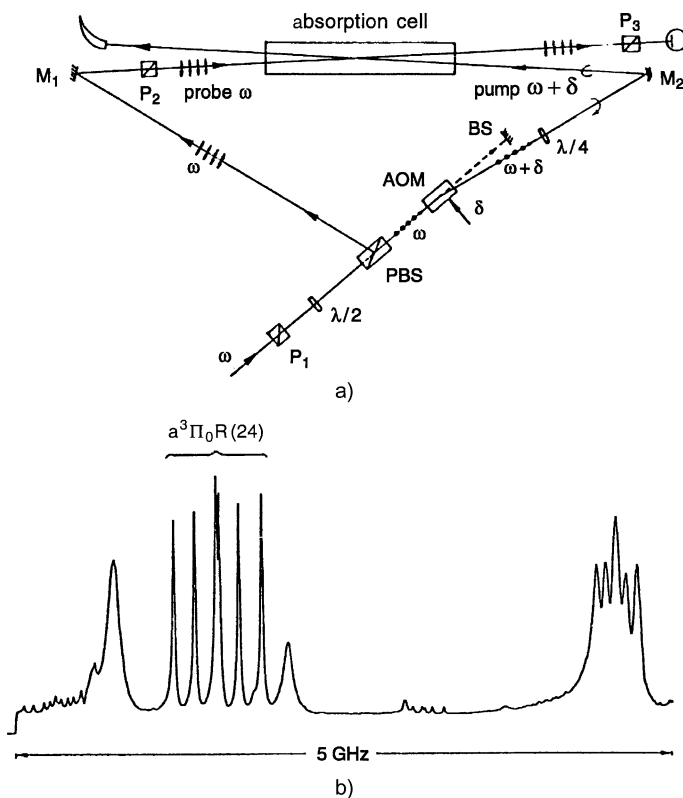


Fig. 2.47 (a) Experimental arrangement of heterodyne polarization spectroscopy; (b) section of the Na_2 polarization spectrum showing the hyperfine splitting of the R(24) rotational line of the spin-forbidden transition $X^1\Sigma_g \rightarrow {}^3\Pi_u$ [276]

through a lock-in device tuned to this frequency, which is chosen in the MHz range. No further chopping of the pump beam is necessary.

2.6.4 Combination of Different Nonlinear Techniques

A combination of Doppler-free two-photon spectroscopy and polarization spectroscopy was utilized by Grützmacher et al. [277] for the measurement of the Lyman- λ line profile in a hydrogen plasma at low pressure.

A famous example of such a combination is the first precise measurement of the Lamb shift in the $1S$ ground state of the hydrogen atom by Hänsch et al. [261]. Although new and more accurate techniques have been developed by Hänsch and coworkers (Sect. 9.7), the “old” technique is quite instructive and shall therefore be briefly discussed here.

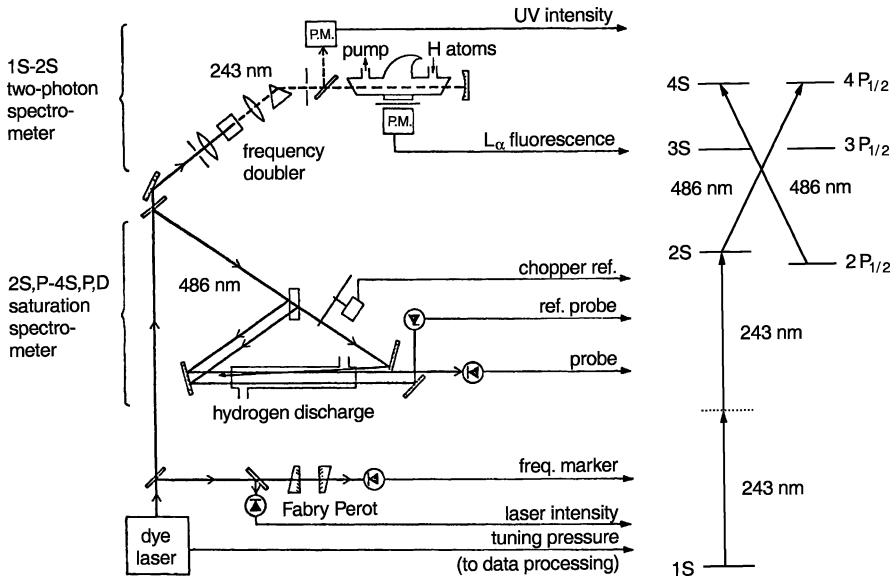


Fig. 2.48 Early experimental setup for measurements of the Lamb shift in the $1S$ state and of the fine structure in the $2P_{1/2}$ state of the H atom by combination of Doppler-free two-photon and saturation spectroscopy [261]

The experimental arrangement is shown in Fig. 2.48. The output of a tunable dye laser at $\lambda = 486 \text{ nm}$ is frequency-doubled in a nonlinear crystal. While the fundamental wave at 486 nm is used for Doppler-free saturation spectroscopy [261] or polarization spectroscopy [278] of the Balmer transition $2S_{1/2} \rightarrow 4P_{1/2}$, the second harmonics of the laser at $\lambda = 243 \text{ nm}$ induce the Doppler-free two-photon transition $1S_{1/2} \rightarrow 2S_{1/2}$. In the simple Bohr model [279], both transitions should be induced at the same frequency since in this model $\nu(1S \rightarrow 2S) = 4\nu(2S \rightarrow 4P)$. The measured frequency difference $\Delta\nu = \nu(1S \rightarrow 2S) - 4\nu(2S \rightarrow 4P)$ yields the Lamb shift $\delta\nu_L(1S) = \Delta\nu - \delta\nu_L(2S) - \Delta\nu_{fs}(4S_{1/2} \rightarrow 4P_{1/2}) - \delta\nu_L(4S)$. The Lamb shift $\delta\nu_L(2S)$ is known and $\Delta\nu_{fs}(4S_{1/2} \rightarrow 4P_{1/2})$ can be calculated within the Dirac theory. The frequency markers of the FPI allow the accurate determination of the hfs splitting of the $1S$ state and the isotope shift $\Delta\nu_{Is}(^1\text{H} \rightarrow ^2\text{H})$ between the $1S \rightarrow 2S$ transitions of hydrogen ^1H and deuterium ^2H (Fig. 2.38).

The more recent version of this precision measurement of the $1S \rightarrow 2S$ transition is shown in Fig. 2.49. The hydrogen atoms are formed in a microwave discharge and effuse through a cold nozzle into the vacuum, forming a collimated beam of color H-atoms. The laser beam is sent through the nozzle and is reflected back anticollinear to the atomic beam axis. The metastable $2S$ atoms fly through an electric field where the $2S$ state is mixed with the $2P$ state. The $2P$ atoms emit Lyman- α fluorescence, which is detected by a solar blind photomultiplier.

If the microwave discharge is pulsed the Lyman α -radiation emitted from the excited H-atoms can be detected behind a time gate as a function of the time de-

Fig. 2.49 Experimental setup for the precise determination of $H(1S \rightarrow 2S)$ frequency [280]

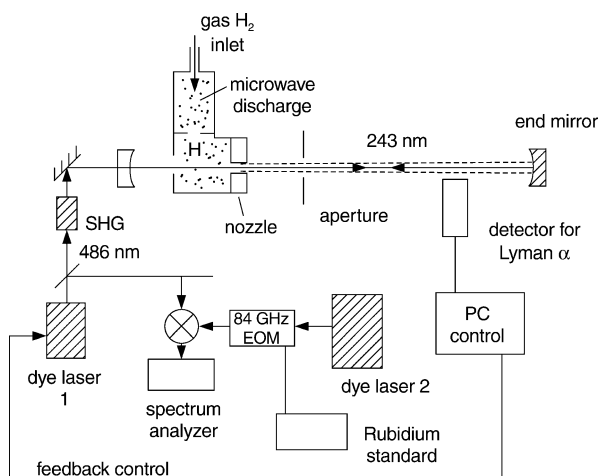
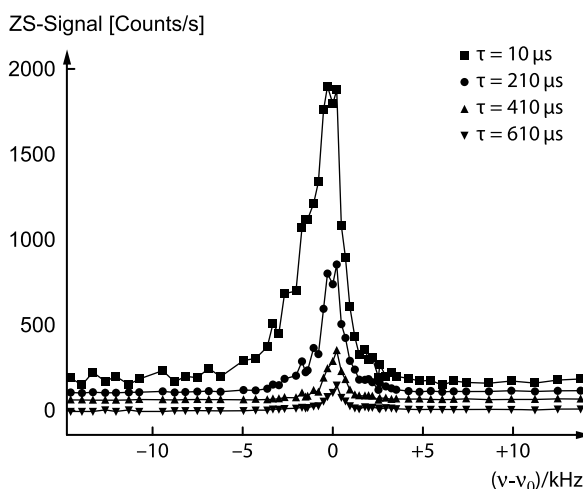


Fig. 2.50 Spectral line profiles of the $1S-2S$ transition measured with Doppler-free two-photon excitation in an atomic hydrogen beam for different atomic velocities



lay between excitation and detection. This allows the selection of different velocity groups of H-atoms. When the laser frequency is tuned over the $1S \rightarrow 2S$ transition the spectral profile of the two-photon transition depends on the second order Doppler-effect (because the first order effect is eliminated by the Doppler-free excitation). This results in a slight shift and asymmetry of the line profiles which become smaller and more symmetric with decreasing atomic velocity (Fig. 2.50). The reason for the asymmetry is the fact, that slow atoms have a longer interaction time with the laser wave and therefore give a larger contribution to the signal.

The achieved relative accuracy of determining the line centre is about 1×10^{-14} . This allows a very accurate determination of the $1S \rightarrow 2S$ transition from which the mean charge radius of the proton can be deduced. Of fundamental importance is the check, whether the fundamental constants change with time. These precision

experiments allow a very small upper limit for a possible variation with time for the values of the fine-structure constant or the Rydberg constant. Tuning the laser frequency over both transitions of hydrogen and deuterium atoms gives an accurate value of the isotope shift of the deuterium atom. The achievable $1S-2S$ linewidth is about 1 kHz, limited by transit-time broadening. The uncertainty of determining the line center is below 30 Hz!

2.7 Conclusion

The few examples shown above illustrate that nonlinear spectroscopy represents an important branch of laser spectroscopy of atoms and molecules. Its advantages are the Doppler-free spectral resolution if narrow-band lasers are used and the possibilities to reach high-lying states by multiphoton absorption with pulsed or cw lasers. Because of its relevance for molecular physics, numerous books and reviews cover this field. The references [203, 205, 281–289] represent only a small selection.

In combination with double-resonance techniques, nonlinear spectroscopy has contributed particularly to the assignment of complex spectra and has therefore considerably increased our knowledge about molecular structure and dynamics. This subject is covered in Chap. 5.

2.8 Problems

2.1

- (a) A collimated sodium beam is crossed by the focussed beam (focal area $A = 0.2 \times 0.01 \text{ cm}^2$) of a single-mode cw dye laser, tuned to the hyperfine component ($F' = 2 \leftarrow F'' = 1$) of the D_2 transition $3^2P_{3/2} \leftarrow 3^2S_{1/2}$ of Na. Calculate the saturation intensity I_s if the mean velocity of sodium atoms is $\bar{v} = 5 \times 10^4 \text{ cm/s}$. The lifetime τ_K of the upper level is $\tau_K = 16 \text{ ns}$ and the residual Doppler width can be neglected.
- (b) How large is I_s in a sodium cell at $P_{\text{Na}} = 10^{-6} \text{ mbar}$ with $P_{\text{Ar}} = 10 \text{ mbar}$ additional argon pressure? The pressure broadening is 25 MHz/mbar for Na–Ar collisions.

2.2 A pulsed dye laser with the pulse length $\Delta T = 10^{-8} \text{ s}$ and with a peak power of $P = 1 \text{ kW}$ at $\lambda = 600 \text{ nm}$ illuminates sample in a cell at $p = 1 \text{ mbar}$ and $T = 300 \text{ K}$. A rectangular intensity profile is assumed with a laser-beam cross section of 1 cm^2 . Which fraction of all N_i in the absorbing lower level $|i\rangle$ is excited when the laser is tuned to a weak absorbing transition $|i\rangle \rightarrow |k\rangle$ with the absorption cross section $\sigma_{ik} = 10^{-18} \text{ cm}^2$? The laser bandwidth is assumed to be 3 times the Doppler width.

2.3 In an experiment on polarization spectroscopy the circularly polarized pump laser causes a change $\Delta\alpha = \alpha^+ - \alpha^- = 10^{-2}\alpha_0$ of the absorption coefficient. By

which angle is the plane of polarization of the linearly polarized probe laser beam at $\lambda = 600 \text{ } \mu\text{m}$ tuned after passing through the pumped region with length L , if the absorption without pump laser $\alpha_0 L = 5 \times 10^{-2}$?

2.4 Estimate the fluorescence detection rate (number of detected fluorescence photons/s) on the Na transition $5s \rightarrow 3p$, obtained in the Doppler-free free-photon experiment of Fig. 2.32, when a single-mode dye laser is tuned to $\nu/2$ of the transition $3s \rightarrow 5s$ ($\nu = 1 \times 10^{15} \text{ s}^{-1}$) in a cell with a Na density of $n = 10^{12} \text{ cm}^{-3}$. The laser power is $P = 100 \text{ mW}$, the beam is focused to the beam waist $w_0 = 10^{-2} \text{ cm}$ and a length $L = 1 \text{ cm}$ around the focus is imaged with a collection efficiency of 5 % onto the fluorescence detector. The absorption cross section is $\sigma = a \cdot I$ with $a = 10^{-10} \text{ W}^{-1}$ and the transition probability of the $5s \rightarrow 3p$ transition is $A_{ki} = 0.2(A_k + R_{\text{coll}})$.

2.5 The saturation spectrum of the Na D_1 transition $3^2S_{1/2} \rightarrow 3^2P_{1/2}$ shows the resolved hyperfine components. Estimate the relative magnitude of the cross-over signal between the two transitions $3^2S_{1/2}(F'' = 1) \rightarrow 3^2P_{1/2}(F' = 1 \text{ and } F' = 2)$ sharing the same lower level, if the laser intensity is 2 times the saturation intensity I_s for the transition to $F' = 1$.

2.6 Which fraction of H atoms in the $1^2S_{1/2}$ ground state that can be excited by a Doppler-free two-photon transition into the $2^2S_{1/2}$ state in a collimated H atomic beam with $\bar{v} = 10^3 \text{ m/s}$, when a laser with $I = 10^3 \text{ W/cm}^2$ and a rectangular beam cross section of $1 \times 1 \text{ mm}^2$ crosses the atomic beam perpendicularly and the absorption probability is $P_{if} = (\sigma_0 \cdot I)^2 / (\gamma \cdot h\nu)^2$ where $\sigma_0 = 10^{-18} \text{ cm}^2$ and γ is the linewidth.

Laser Spectroscopy 2

Experimental Techniques

Demtröder, W.

2015, XXII, 759 p. 582 illus., Hardcover

ISBN: 978-3-662-44640-9